McMaster University

Masters Thesis

High Field NMR Investigation of $Yb_2Pt_2O_7$

Author:
Sean Kentaro Sullivan Takahashi

Supervisor:
Dr. Takashi Imai

A thesis submitted in fulfilment of the requirements for the degree of Masters of Science

in the

Department of Physics

August 2017

McMASTER UNIVERSITY

Abstract

Department of Physics

Masters of Science

High Field NMR Investigation of $Yb_2Pt_2O_7$

by Sean Kentaro Sullivan TAKAHASHI

The rare-earth pyrochlore oxides are the prime example of three-dimensional frustrated magnetism. Pyrochlores are of the chemical form $A_2B_2O_7$ where the A site is a rare-earth metal and B is a non-magnetic ion. The A and B sites separately form a network of corner-sharing tetrahedra which are interwoven with each other. The geometric frustration of the pyrochlores make them extremely interesting as it introduces new and complicated behaviour that has not been studied before. It is typically difficult to conduct NMR experiments on such materials as many of the more well studied pyrochlore materials do not have appropriate nuclei for NMR. $Yb_2Pt_2O_7$ is an exception as platinum is an excellent atom for NMR experiments. $Yb_2Pt_2O_7$ is considered an effective S=1/2 XY pyrochlore, meaning that the magnetic moment on the Yb ion is anisotropic. we performed ^{195}Pt high field NMR measurements on a powder sample of the pyrochlore $Yb_2Pt_2O_7$ in fields from 1 T to 8 T. The NMR frequency shift increased rapidly at low temperature until it was saturated due to the magnetic field strength. The spin-lattice relaxation rate, $1/T_1$, showed exponential behaviour from 20 K down to 1.8 K for the higher fields of 2 T, 4 T and 8 T. The rapid decrease in $1/T_1$ indicates that the low frequency spin fluctuations freeze out at temperatures well before the known zero-field transition to a ferromagnetic state at 0.3 mK. We fitted the $1/T_1$ data to an exponential $e^{-\Delta/T}$ to extract an energy scale Δ. Alternatively, we also used the peak of the $1/T_1T$ data as a function of temperature and scaling analysis to determine an energy scale. All three methods showed semi-quantitatively the same behaviour with magnetic field strength, where Δ decreases linearly as the field strength is lowered. Low field NMR experiments are being planned to determine if this behaviour continues below 1T.

Acknowledgements

Dr. Takashi Imai for his expertise in the fields of NMR and condensed matter physics. None of this would be possible without his guidance and ability.

Dr. Paul Dube for consistently ensuring our cryogenic systems remain cold.

Annica Freytag for proofreading and helping me get through the writing process.

Alex Arsenault for assisting with many of the experiments conducted for this thesis and being an excellent lab partner.

Alannah Hallas for allowing us to use the $Yb_2Pt_2O_7$ sample she made. As one of the experts on pyrochlores, she also provided helpful conversations on the subject

Jonathan Gaudet for helpful communications about the pyrochlores.

My family for supporting my endeavors and not giving up on me.

Contents

Abbreviations

CEF	**C**rystalline **E**lectric **F**ield
FID	**F**ree **I**nduction **D**ecay
HPHT	**H**igh **P**ressure and **H**igh **T**emperature
LD	**L**ong **D**elay
μSR	**M**uon **S**pin **R**elaxation
NMR	**N**uclear **M**agnetic **R**esonance
QSL	**Q**uantum **S**pin **L**iquid
RF	**R**adio **F**requency

Chapter 1

Rare Earth Pyrochlore Oxides

1.1 Motivation

Of all the research fields in science, there is perhaps no better field than condensed matter physics that demonstrates the interplay between theory, experiment and technology. Experimental discoveries have driven theorists to develop intricate and elegant methods of explaining physical phenomena, while theorists have force experimentalists to hone their techniques in order to observe predicted behaviour in many systems. Technology has benefitted greatly from the discoveries in the field, which has, in turn, aided the developement of increasingly advanced experimental equipment.

Condensed matter physics is a vast and deep field of study that has driven science and technology forward over the past century. The theory behind semiconductors, was developed in the wake of the discovery of quantum mechanics. Bardeen et al. created the first semiconductor transistor in 1948 [1] which brought a revolution to computing and electronics. Shortly after in 1957, one of the triumphs in modern physics occured: Bardeen, Cooper and Schriefer laid the groundwork for a microscopic theory of superconductivity [2].

The study of magnetism in materials eventually led to the creation of magnetic storage devices such as hard drives in computers. In the 1960s and 70s, critical phenomena and the renormalization group were rigorously developed which now plays an important role in both condensed matter physics and quantum field theory [3]. The discovery of the high T_c cuprate superconductor $Ba_xLa_{5-x}Cu_5O_{5(3-y)}$ in 1986 by Bednorz and Müller

[4] was a major boost for the field, as people imagined the possibility of eventually reaching room-temperature superconductivity. Since that time, although modifications have been made to reach higher T_c's, we are still a long ways off of reaching the ultimate goal of room temperature superconductivity. In order to attempt to explain the high temperature superconductors, studies of many different materials have been undertaken.

At about the same time the high T_c superconductors were taking the physics world by storm, another phenomena was gathering steam in condensed matter: magnetic and geometric frustration. Although frustration had already been theoretically discussed [5], [6] [7], a very special class of frustrated materials, the pyrrochlore oxides, had yet to be analyzed in depth. The pyrochlore oxides epitomize 3-dimensional geometric frustration and have now been rigorously studied. They have become an entirely separate research field for the study of magnetism. Pyrochlores have already made important discoveries for condensed matter discussed briefly in the next section, with more discoveries potentially on the way. We will gain a greater understanding of condensed matter systems and physics overall by understanding the complex behaviour of pyrochlores.

1.2 The Pyrochlore Structure

The pyrochlore oxides are crystal structures of the form $A_2B_2O_7$. Both the A and B sites form sublattices of corner-sharing tetrahedra which are interwoven with each other; as shown in 1.1. The oxygen atoms sit between the atoms of the A and B sub-lattices. When mentioning the pyrochlore structure from this point onward, it will be referring to the pyrochlore oxide structure as a whole. Pyrochlore oxides can exhibit many physical states including insulating, metallic and superconducting states, depending on the atoms occupying the A and B sites [8]. Pyrochlore lattices are particularly interesting in magnetism because they exhibit geometric frustration when one of the A or B sites contains a magnetic ion. Geometric frustration occurs when the configuration of the magnetic moments in the lattice affects the ground state energy of the system, such that neighbouring spins cannot align in their most energetically preferred position in their ground state [5], [9]. In the pyrochlore oxides, magnetic frustration leads to some exotic physical phenomena such as spin ices in $Ho_2Ti_2O_7$ [10] [11] and $Dy_2Ti_2O_7$ [12], cooperative paramagnetism in $Tb_2Ti_2O_7$ [13], spin glass state in $Yb_2Mo_2O_7$ [14] and $Tb_2Mo_2O_7$ [15] as well as others which have been studied extensively [16].

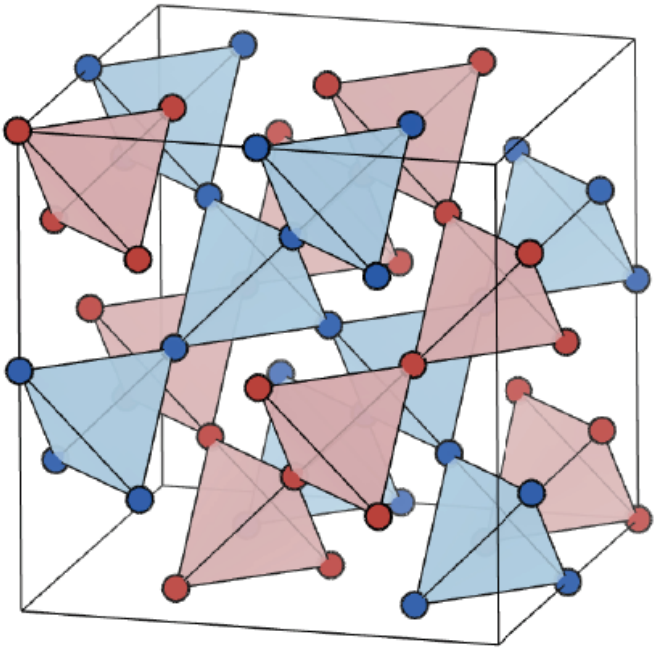

FIGURE 1.1: Pyrochlore network of A and B sites from [17]. Another way of thinking about the structure is alternating layers of kagome and triangular lattices for both the A and B sites. The kagome layers of the A site are in the same plane as the triangular layers of the B site.

Figure 1.2 from reference [18] a) shows two corner-sharing Gd tetrahedra from $Gd_2Pt_2O_7$. The center gadolinium ion is surrounded by 8 oxygens and a hexagon of platinum ions. In figure 1.2 b) the platinum site is surrounded by a hexagon of oxygens which are bonded to a hexagon of gadolinium. It is not always the case that the oxygen atoms sit perfectly in plane with the b-site. In fact, in $Yb_2Ti_2O_7$ the oxygen ions are alternating above and below the plane [19].

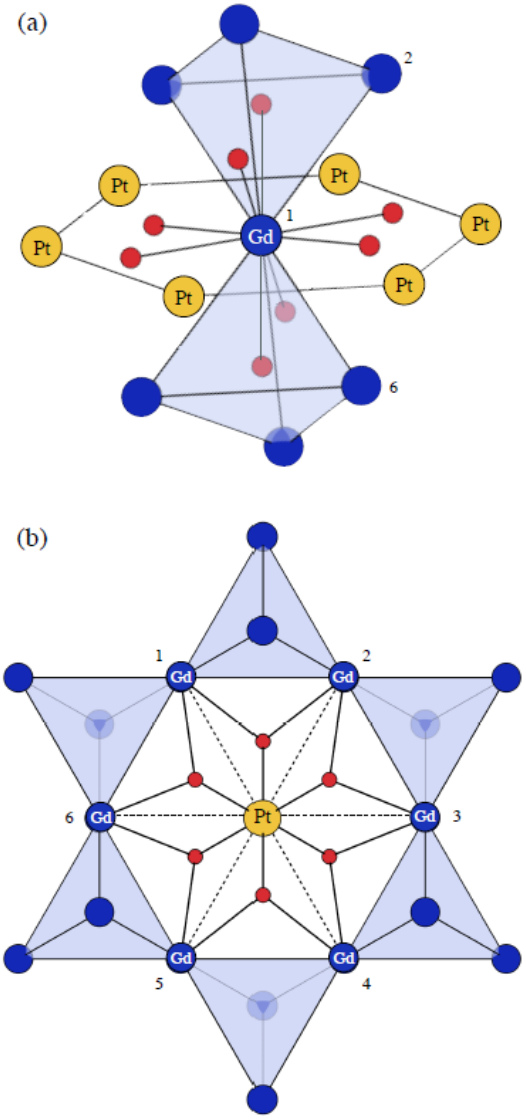

FIGURE 1.2: a) Two corner-sharing tetrahedra of gadolinium in $Gd_2Pt_2O_7$. b) View down the local [111] axis of platinum site in $Gd_2Pt_2O_7$. The structure will be discussed in more detail in the next section. Figures taken from [18].

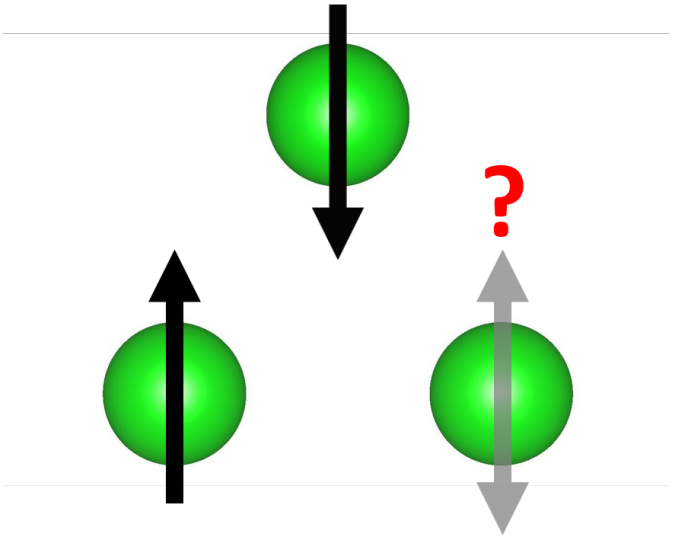

FIGURE 1.3: A triangle of antiferromagnetic Ising spins. When two of the spins align antiferromagnetically, the third spin is in a frustrated state.

The typical example of geometric frustration is three antiferromagnet Ising spins forming an equilateral triangle. There is no configuration where all three spins are satisfied as if two spins point opposite to each other, the third spin will not have a preference to point up or down. It is in a frustrated state as seen in 1.3. This introduces a degeneracy in the lowest energy (ground) state. Expanding the frustrated triangle to a lattice can produce a triangular lattice (edge-sharing triangles) or a kagome lattice (corner-sharing triangles). Generalizing to three dimensions, the base unit is a tetrahedron which can also be edge-sharing which makes a face-centred cubic lattice (FCC) or corner-sharing which makes the pyrochlore lattice.

Since there is geometric frustration in a network of triangles, there should also be frustration in the more generalized 3-dimensional network of corner-sharing tetrahedra. This frustration can lead to the celebrated spin ice state, so called because the behaviour of the magnetic moments on the tetrahedra sites resemble the disorder of hydrogen atoms in water ice as shown in figure 1.4. The "ice rule" of water ice states that each oxygen will be bonded with four hydrogen atoms, but that two of these bonds will be weak and two will be strong, *i.e.* two hydrogens sit close to the oxygen, while the other two sit further away [21]. This introduces a degeneracy in the ground state as there are many combinations of bonds which minimize the energy of the system. Thus, there is residual entropy, *i.e.* non-zero entropy in its ground state [22]. In a two state system

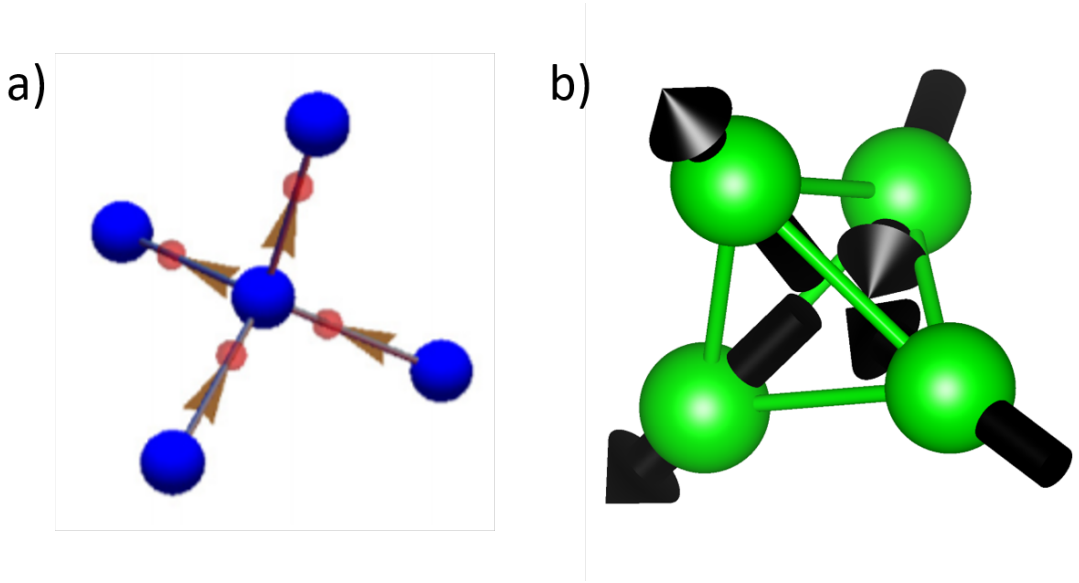

FIGURE 1.4: a) Arrangement of protons (red) in water ice relative to oxygen (blue) [20]. Two protons are close to the centre of the structure, but two are closer to the outer oxygens. b) Example of how frustrated spins may arrange themselves on a tetrahedra. Two of the spins point into the tetrahedra and two of them point outwards. This is the 2 in 2 out ice rule.

this becomes $S = R\ln(2)$ per site where R is the gas constant. In a pyrochlore spin ice, the geometric frustration leads to two of the spins on a tetrahedra pointing into the tetrahedra while two of the spins outwards (also known as the two in two out rule) which also leads to residual entropy [23].

In recent years, the ytterbium and erbium based pyrochlores have garnered a great amount of interest and academic resources due to their XY spin nature. It has been shown that for the ytterbium and erbium based pyrochlore oxides, the anisotropic g-tensors have a larger perpendicular component than parallel ($g_\perp > g_\parallel$) [24] [25] [26] [27] [28] [29]. For example, in the case of $Yb_2Ti_2O_7$, $g_\perp = 3.69 \pm 0.15$ and $g_\parallel = 1.92 \pm 0.20$ as measured by Gaudet et. al. [27]. The XY anisotropy arises from the crystalline electric field (CEF), which is originates strongly from the oxygen sites. The XY pyrochlores have led to some interesting discoveries such as the continuous phase transition to an ordered stated of $Er_2Ti_2O_7$ [30] [31] which is thought to be achieved via the order-by-disorder mechanism. In addition, if spin ices exist on XY pyrochlores, they will potentially be quantum spin ices which differ from the classical spin ices of $Ho_2Ti_2O_7$ and $Dy_2Ti_2O_7$ previously mentioned, as they are driven by quantum fluctuations.

1.3 $Yb_2Pt_2O_7$

The $Yb_2Pt_2O_7$ powder sample was synthesized under high pressure and high temperature (HPHT) by Alannah Hallas, and is thermally stable once it is formed [32]. The ionic radii of Yb^{3+} and Pt^{4+} are 0.868 $\AA$ and 0.625 $\AA$ respectively [33], so that their ratio is, $IR_A/IR_B = 1.39$. This is within the range of stable pyrochlore materials of $1.36 \leq IR_A/IR_B \leq 1.71$ at ambient temperature and pressure [34]. The structure is as shown in figure 1.7 where corner-sharing tetrahedra lattices of Yb and Pt are interwoven with each other.

The Yb^{3+} site is pseudospin $S = 1/2$ with XY anisotropy perpendicular to the local [111] axis [35]. Since this is defined on the local axis, the XY spins are not necessarily in the same plane.

In the absence of dipolar interactions, the nearest neighbour exchange Hamiltonian can be written as the following from reference [36]

$$H = \frac{1}{2}\sum_{ij} J_{ij}^{\mu\nu} S_i^{\mu} S_j^{\nu} - \mu_B H^{\mu} \sum_i g_i^{\mu\nu} S_i^{\nu}, \tag{1.1}$$

where $J_{ij}^{\mu\nu}$ are matrices which describe the exchange couplings between sites i and j, H^{μ} is the magnetic field strength and direction and $g_i^{\mu\nu}$ is the g-tensor for the spin S at site i. There are four independent exchange coupling constants (J_1, J_2, J_3 and J_4). Since the ytterbium site has strongly localized f-electron states, only considering nearest neighbour interactions is justified [36]. Equation 1.1, in the zero field case, may be rewritten for spins quantized in the local [111] direction as the following:

$$H = \sum_{\langle i,j \rangle} [J_{zz} S_i^z S_j^z - J_{\pm}(S_i^+ S_j^- + S_i^- S_j^+) + J_{\pm\pm}(\gamma_{ij} S_i^+ S_j^+ + \gamma_{ij}^* S_i^- S_j^-) + J_{z\pm} S_i^z (\xi_{ij} S_j^+ + \xi_{ij}^* S_j^-) + i \rightarrow j]. \tag{1.2}$$

In equation 1.2, there are four independent exchange constant: J_{zz}, $J_{\pm}$, $J_{\pm\pm}$ and $J_{z\pm}$. These are related to J_1, J_2, J_3 and J_4 by the following relations [36].

$$J_{zz} = -\frac{1}{3}[2J_1 - J_2 + 2(J_3 + 2J_4)], \tag{1.3}$$

$$J_{\pm} = \frac{1}{6}[2J_1 - J_2 - J_3 - 2J_4], \tag{1.4}$$

$$J_{\pm\pm} = \frac{1}{6}[J_1 + J_2 - 2J_3 + 2J_4], \tag{1.5}$$

$$J_{z\pm} = \frac{1}{3\sqrt{2}}[J_1 + J_2 + J_3 - J_4]. \tag{1.6}$$

The S_i^{μ} are local spin coordinates and γ_{ij} and ξ_{ij} are unimodular matrices of complex numbers. In the case of $Yb_2Ti_2O_7$, $J_{\pm\pm}$ and $J_{\pm}$ have been estimated to be on the order of ~ 0.5 meV and $J_{z\pm} \sim 0.15$ meV [36] [37]. Ross et al. quote $J_{zz} = 0.17 \pm 0.04$ meV while Thompson et al. quote it as $J_{zz} = 0.026 \pm 0.03$ meV. In any case, the exchange interactions are generally quite small at below 1 meV.

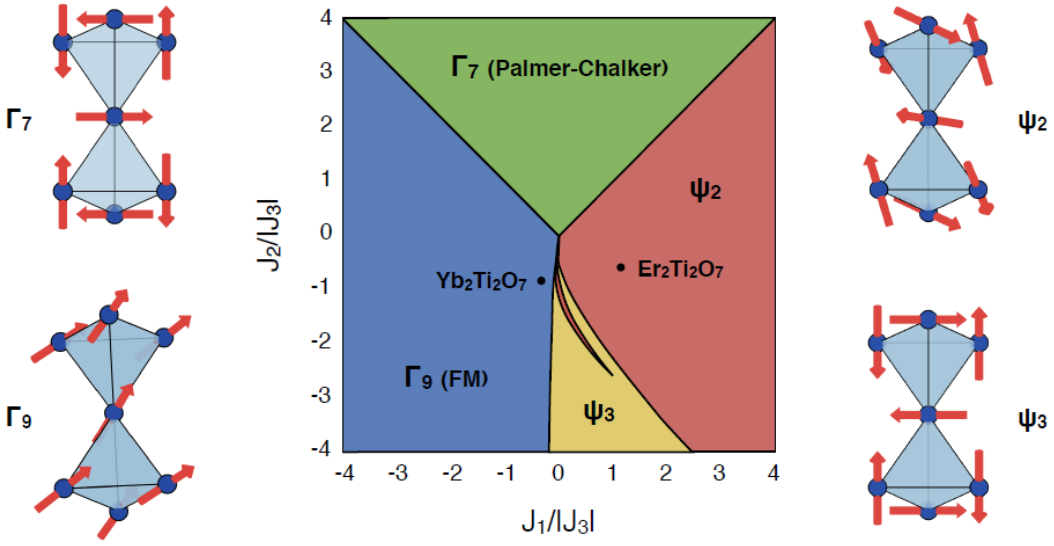

FIGURE 1.5: Phase diagram of the spin configurations of pyrochlores with anisotropic exchange from [17]. The exchange parameters for $Yb_2Ti_2O_7$ were determined by [36] and $Er_2Ti_2O_7$ were determined by [38].

Figure 1.5 from reference [17] shows the phase diagram for the spin configurations of anisotropic exchange in XY pyrochlores. The exotic magnetic properties are thought to arise from phase competition [39]. Although $Yb_2Pt_2O_7$, which is the subject of this thesis, has not had its spin configuration determined, it is known to be ferromagnet at low temperatures, much like $Yb_2Ti_2O_7$.

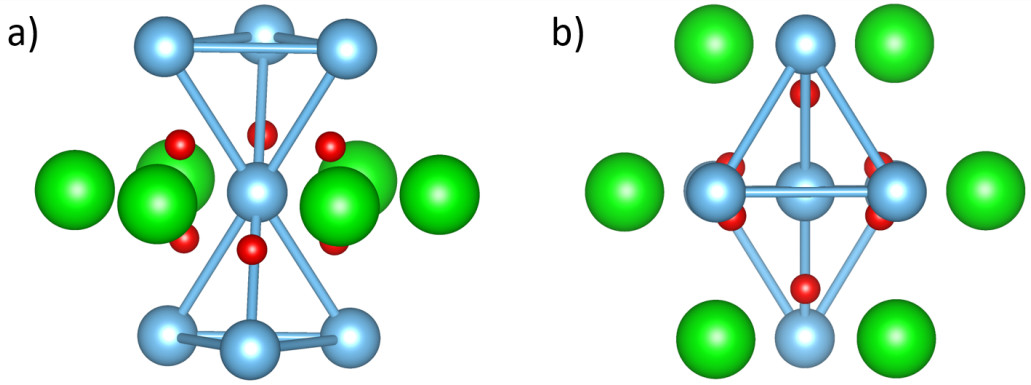

FIGURE 1.6: a) view of platinum site (blue) surrounded by a hexagon of ytterbium ions (green). The oxygen ions (red) are situated in between the platinum and ytterbium sites. b) view along the local [111] axis of the same platinum site.

.

^{195}Pt is an excellent nuclei for NMR with many advantages. First, it has a relatively high gyromagnetic ratio of 9.153 MHz/T. On the other hand, the more well studied titanates would require NMR on ^{47}Ti or ^{49}Ti, both with gyromagnetic ratio of about 2.40 MHz/T [40]. To achieve the same signal to noise ratio as ^{195}Pt, we would need a field almost 4 times larger. As will be discussed in chapter 2, the resonance frequency of a nuclei is proportional to the magnetic field applied. The low field NMR frequency of titanium is too low for NMR experiments. Second, since ^{195}Pt has nuclear spin $I = 1/2$, it does not have a nuclear quadrupole moment, and thus there is a single NMR line peak. ^{47}Ti and ^{49}Ti are $I = 5/2$ and $I = 7/2$ nuclei respectively, which would result in 5 peaks in the ^{47}Ti NMR lineshape and 7 in the ^{49}Ti Lineshape. As a sidenote, another previously studied pyrochlore $Yb_2Ge_2O_7$ has germanium with nuclear spin $I = 9/2$ so 9 peaks in the NMR lineshape. The third advantage of ^{195}Pt NMR is its relatively high natural abundance of 33.7% compared to 5.5% and 7.3% for ^{47}Ti and ^{49}Ti respectively. Metallic pyrochlores such as the ruthenates [41] [42] and rhenates [43] have been studied via NMR, however, insulating pyrochlore oxides such as the titanates, germanates and platinates have not been examined in depth with NMR as far as we know.

The Pt^{4+} site is surrounded by a hexagon of Yb^{3+} ions, separated by oxygen ions as shown in figure 1.6. It is in a low spin ($t_{2g}^6 e_g^0$) state and is nonmagnetic. This is good for our NMR experiments as we would like to determine how the Yb^{3+} moments behave by probing the ^{195}Pt nuclei. It is, in principle, possible to conduct ytterbium NMR as

^{171}Yb is nuclear spin $I = 1/2$ and $\gamma_N = 7.52$ MHz/T [40]. However, since ytterbium is in a magnetic environment [35], the hyperfine coupling constant (A_{hf}) will be quite large. As will be seen in chapter 2, the NMR frequency shift is proportional to A_{hf} and the spin-lattice relaxation rate is proportional to A_{hf}^2/J. Thus, highly magnetic sites require an extremely large frequency range and incredibly fast resolution in order to conduct NMR experiments, unless J is quite large as well. It is therefore much easier to work with the non-magnetic ^{195}Pt site.

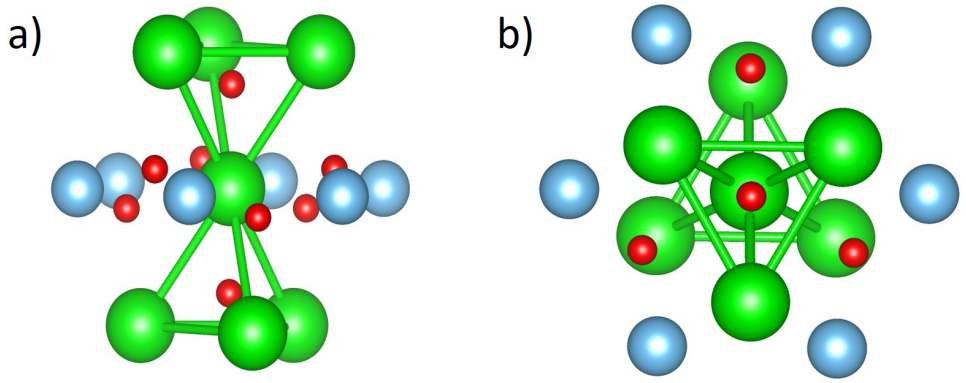

FIGURE 1.7: a) The corner-sharing tetrahedra of the magnetic A site (green) in relation to the nearest oxygen atoms (red) and the non-magnetic B sites (blue). b) View down the local [111] axis of two corner sharing ytterbium tetrahedra.

Figure 1.7 shows that the B sites make a hexagon around the joining of two A site tetrahedra. Oxygen atoms are in between the platinum and ytterbium sites as well as near the middle of the tetrahedra. The moment from the ytterbium site can be transferred to the platinum by hybridization. This results in hyperfine coupling between the ytterbium magnetic moment and the platinum nuclear spin.

Previous studies of $Yb_2Pt_2O_7$ have shown that it is paramagnetic with a transition to long-range ferromagnet order at 0.3 K as noted in figure 1.8. Cai, et al determined $\theta_{CW} = 0.91$ K and $\mu_{eff} = 3.08\mu_B$ [35]. Both $Yb_2Pt_2O_7$ and $Yb_2Ti_2O_7$ have a specific heat anomaly which occurs around 2 K as seen in figure 1.8. This specific heat anomaly is generally not well explained, but could be linked to the spin configuration of the system.

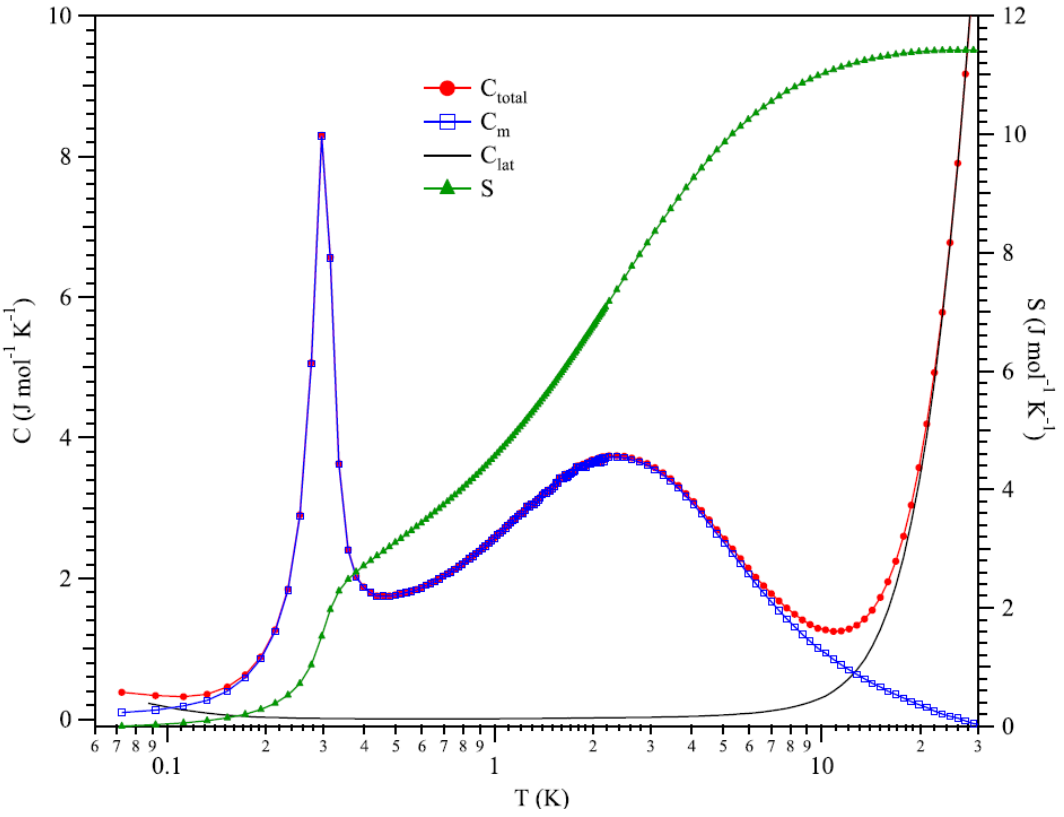

FIGURE 1.8: Zero field specific heat measurements for $Yb_2Pt_2O_2$ as reported in [35]. The red data points are the total specific heat, while C_m is the magnetic specific heat and the black line is the lattice contribution to the specific heat. There is a broad bump in the total specific heat centered around 2 K which is clearly not the transition to long-range order that occurs 0.3 K. The green data points are calculated entropy from the specific heat measurements by integrating over C_m/T.

Figure 1.8 also shows that the the entropy levels off at 11.42 J mol^{-1} K^{-1}, almost exactly the ideal value for the entropy in a spin $S = 1/2$ system of $S = 2R\ln(2)$. This confirms that the Yb^{3+} moment can be treated as a pseudospin $S = 1/2$, which is the same as other previous studies of ytterbium pyrochlores with different non-magnetic sites, such as $Yt_2Ti_2O_7$ [19] [44], $Yt_2Sn_2O_7$ [45] and $Yt_2Ge_2O_7$ [46].

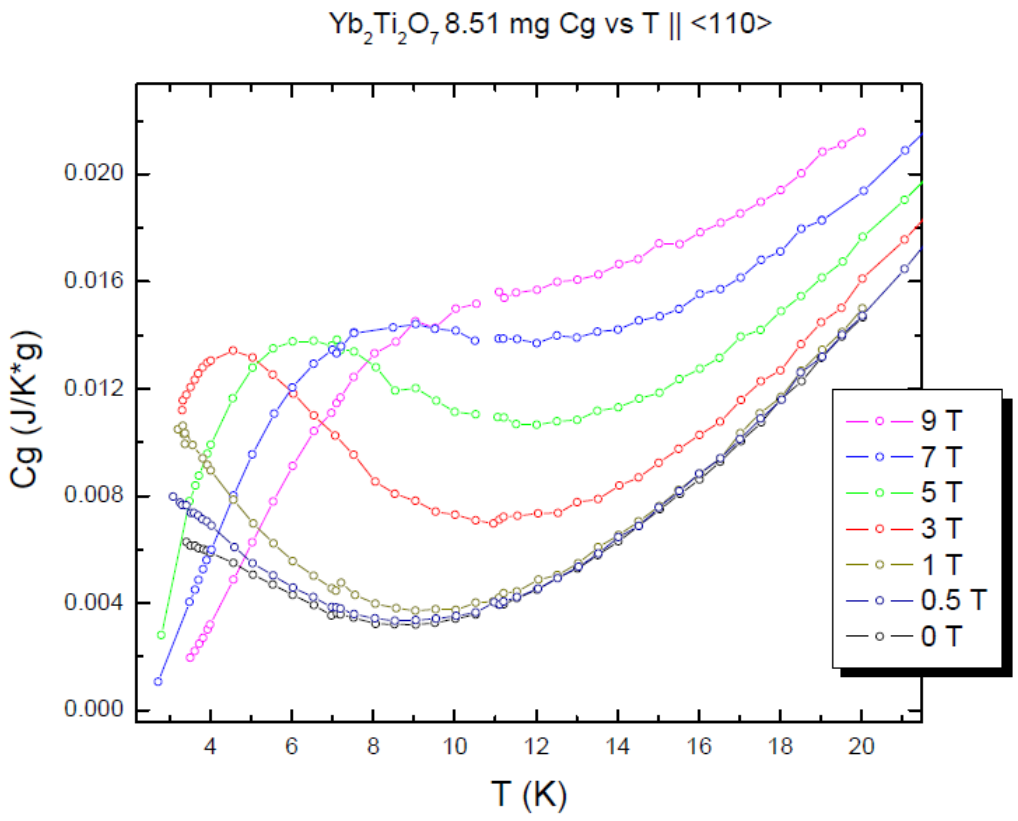

FIGURE 1.9: Specific heat measurements of $Yb_2Ti_2O_7$ at different fields as completed by D'Ortenzio [47]

The location of the peak of the broad specific heat anomaly in the sister compound $Yb_2Ti_2O_7$ scales roughly linearly with magnetic field above 1T, as mentioned in Robert D'Ortenzio's thesis (see figure 1.9). More recently, Thompson et al. extracted an energy scale from the specific heat data by fitting it to a Schottky profile for a two level system. This was completed at low fields and they argued that this scale changes monotonically with magnetic field [37]. The energy scale does not show linear behaviour below 0.4 T however, but decreases more quickly with decreasing field. It should be noted that Thompson et al. applied the field in the [001] crystallographic direction while D'Ortenzio applied the fields in the [110] and [100] directions. D'Ortenzio found that there was no difference in the specific heat between the [110] and the [100] directions.

Along with this unexplained specific heat anomaly, rare-earth pyrochlore oxides can theoretically exhibit properties of quantum spin liquids (QSL) as predicted in [36]. QSL is a highly sought after exotic state and examining $Yb_2Pt_2O_7$ via NMR will shed light

on the magnetic properties of the XY pyrochlores as a family to hopefully understand the complex behaviour of XY pyrochlore systems.

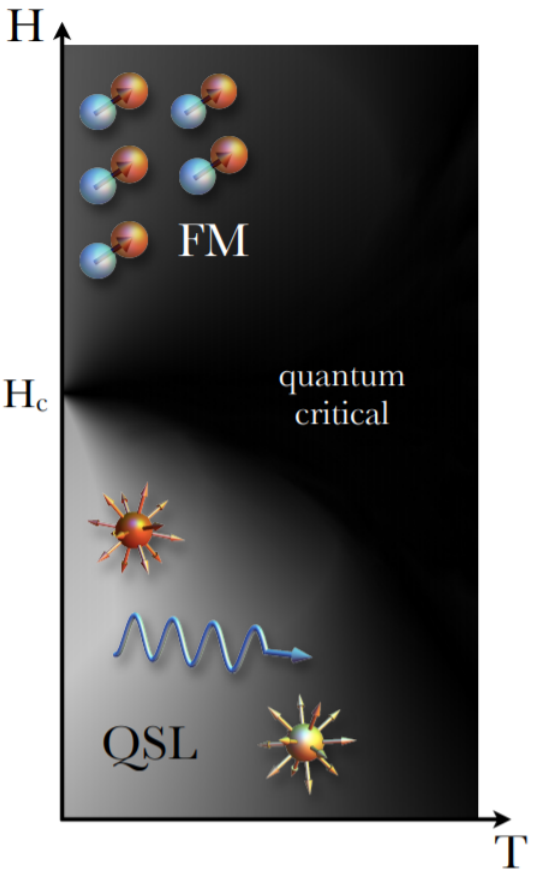

FIGURE 1.10: It is theoretically possible for a pyrochlore to become a QSL when $J_{\pm}/J_{zz}$ is sufficiently small [36]. Phase diagram from Ross et al. [36].

In this thesis, we examine the high field (1T and above) behaviour of $Yb_2Pt_2O_7$ using NMR. As mentioned previously, some of the more studied pyrochlore oxides such as the titanates and germanates are not ideal for NMR and as a result, there are very few NMR studies on these particular pyrochlores oxides. This NMR study is the first of its kind on the pyrochlore oxides and aims to understand how the specific heat anomaly is related to the magnetic properties, among other things. Since NMR is a low energy probe, it is perfect for investigating low energy excitations that other probes may not be able to achieve. NMR thus makes an excellent complimentary tool for higher energy probes such as neutron scattering and muon spin relaxation μSR.

Chapter 2

NMR Basics

2.1 Resonance Theory

In the classical picture of spin, a spin is a magnetic moment pointing in a certain direction in space. Consider an isolated magnetic moment $\boldsymbol{\mu}$ in an external magnetic field $\boldsymbol{B_0} = B_0 \times \hat{\boldsymbol{z}}$, where $\hat{\boldsymbol{z}}$ denotes the unit vector in the direction of z. Vector quantities are defined with bold font. The magnetic field exerts a torque $\boldsymbol{\tau}$ on the moment given by the following.

$$\boldsymbol{\tau} = \boldsymbol{\mu} \times \boldsymbol{B_0}. \tag{2.1}$$

In this simple model, the magnetic moment would want to align with the magnetic field, leading to Larmor precession about the field direction (if the moment did not already start pointing along the field direction). These oscillations obviously die out if there is some damping term.

A nucleus with an odd number of neutrons and/or protons possesses an angular momentum $\boldsymbol{I}$. Since the rate of change of angular momentum with respect to time is the torque, we may equate this to equation 2.1 and obtain the equation of motion for the magnetic moment.

$$\frac{d\boldsymbol{I}}{dt} = \boldsymbol{\mu_N} \times \boldsymbol{B_0}. \tag{2.2}$$

The convenient fact that $\boldsymbol{\mu}$ and $\boldsymbol{I}$ are either parallel ($\boldsymbol{\mu_N} > 0$) or antiparallel ($\boldsymbol{\mu_N} < 0$) allows us to relate them with a constant scalar such that $\boldsymbol{\mu} = \gamma_N \boldsymbol{I}$ where γ_N is the nuclear gyromagnetic ratio. Then we can eliminate $\boldsymbol{I}$ from equation 2.2.

$$\frac{d\boldsymbol{\mu}}{dt} = \boldsymbol{\mu} \times \gamma_N \boldsymbol{B_0} \tag{2.3}$$

An important consequence of this equation is that the instantaneous change in $\boldsymbol{\mu}$ is always perpendicular to the applied field and $\boldsymbol{\mu}$. For the time independent zero damping case, $\boldsymbol{\mu}$ will then trace out a cone around $\boldsymbol{B_0}$ of a constant angle. In reality, there will be damping coming into the system which will be discussed later.

In general, we can move into a rotational frame where the system coordinates rotate at constant angular velocity $\boldsymbol{\Omega}$. It is then not hard to show that equation 2.3 becomes

$$\frac{\partial \boldsymbol{\mu}}{\partial t} = \boldsymbol{\mu} \times (\gamma_N \boldsymbol{B_0} + \boldsymbol{\Omega}) \tag{2.4}$$

This means that we can treat the rotational frame the same way as the static frame as long as we replace the magnetic field with an effective field $\boldsymbol{B_{eff}} = \boldsymbol{B_0} + \frac{\boldsymbol{\Omega}}{\gamma_N}$. Choosing $\boldsymbol{B_{eff}} = 0$ requires $\frac{\partial \boldsymbol{\mu}}{\partial t} = 0$ so that $\boldsymbol{\mu}$ rotates with angular velocity $\boldsymbol{\Omega} = -\gamma_N B_0 \hat{\boldsymbol{z}}$. We can use this to define a characteristic frequency of the system.

$$\omega_L = \gamma_N B_0 \tag{2.5}$$

ω_L is the Larmor frequency, which is the frequency at which the magnetic moment precesses about the magnetic field in the rotational reference frame.

Using a quantum mechanical description of a spin in the static field, the magnetic moment interacts with the magnetic field by the Zeeman interaction.

$$\mathcal{H} = -\boldsymbol{\mu} \cdot \boldsymbol{B_0} = -\gamma_N \hbar B_0 I_z. \tag{2.6}$$

The allowed energies of the system are therefore just the Zeeman levels.

$$E = -\gamma_N \hbar B_0 m, \tag{2.7}$$

where $m = I, I-1, \ldots, -I$. Magnetic dipole transitions are allowed between adjacent energy levels. We can probe the system by applying a field at a frequency such that $\hbar\omega = \Delta E$ to induce a transition between the levels.

2.2 NMR Experiments

NMR experiments are versatile, and there are many ways one can utilise NMR. In this thesis, we will report pulsed NMR experiments completed in an external field. The simplest experiment one can perform with these conditions is a free induction decay (FID). In this scenario, the sample is exposed to an oscillating magnetic field $\boldsymbol{B}_1$, perpendicular to the external magnetic field, $\boldsymbol{B}_0$. Thinking of the nuclear spins classically, when $\boldsymbol{B}_1$ is turned on, they will precess around the effective magnetic field [48]:

$$\boldsymbol{B_{eff}} = (B_0 - \frac{\omega}{\gamma_{\mathrm{N}}})\hat{\boldsymbol{z}} + B_1\hat{\boldsymbol{x}} \tag{2.8}$$

Equation 2.8 assumes that B_0 is in the z-direction and B_1 is in the x-direction in the rotational frame. When the resonance condition is exactly met, *i.e.* $\omega = \gamma_{\mathrm{N}} B_0$, then the nuclear spin will rotate in the y-z plane. This is convenient, as we can now manipulate the direction of the nuclear spin as we please. In order to flip the spin from the z-direction to the x-y plane, we simply need to turn $\boldsymbol{B}_1$ on for a specific duration of time to flip the spin 90°.

$$\frac{\pi}{2} = \omega_1 t_{90} = \gamma_{\mathrm{N}} B_1 t_{90} \tag{2.9}$$

t_{90} is typically on the the order of 3-8μs for our condensed matter experiments. Upon turning off the pulse after time t_{90}, the spins would be pointing in the y-direction and precessing around the z-axis. As the spins precess, the net magnetization of the sample precesses as well. This precession takes place in a coil perpendicular to the external magnetic field. Since the precession induces an oscillating voltage in the coil, a measureable

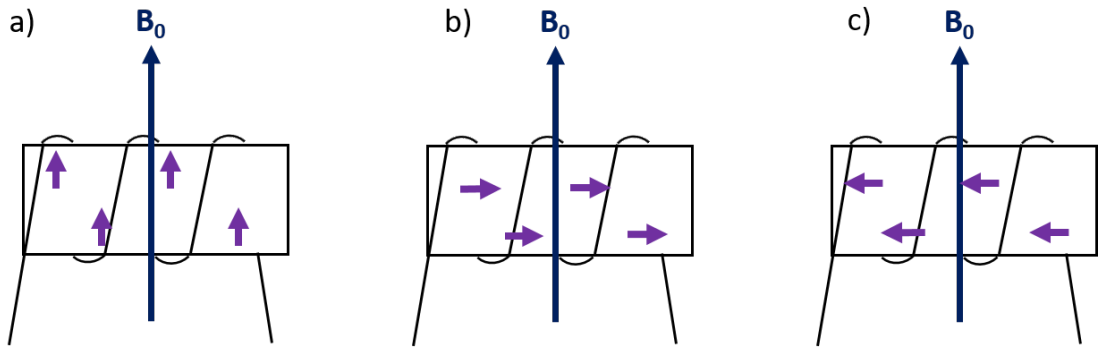

FIGURE 2.1: a) The sample is placed in a solenoid. In thermal equilibrium, the net magnetic moment will point along the $\boldsymbol{B}_0$ direction. b) A 90° pulse is applied, flipping the spins into the x-y plane. c) The spins precess perpendicular to $\boldsymbol{B}_0$ causing the net magnetization of the sample to precess. In accordance to Farraday's law, this induces a measureable oscillating voltage in the solenoid at the Larmor precession frequency.

signal (called the FID signal) is produced. This simple experiment, in principle, can be completed using solenoid for both applying $\boldsymbol{B}_1$ and recording the precession of the net magnetization as shown in figure 2.1. The signal oscillates at the resonant frequency of the sample which is on the order of tens of MHz (period of $\sim 0.1\mu$s). This is quite short in the time domain, so we only record the envelope function of the signal and use that for analysis.

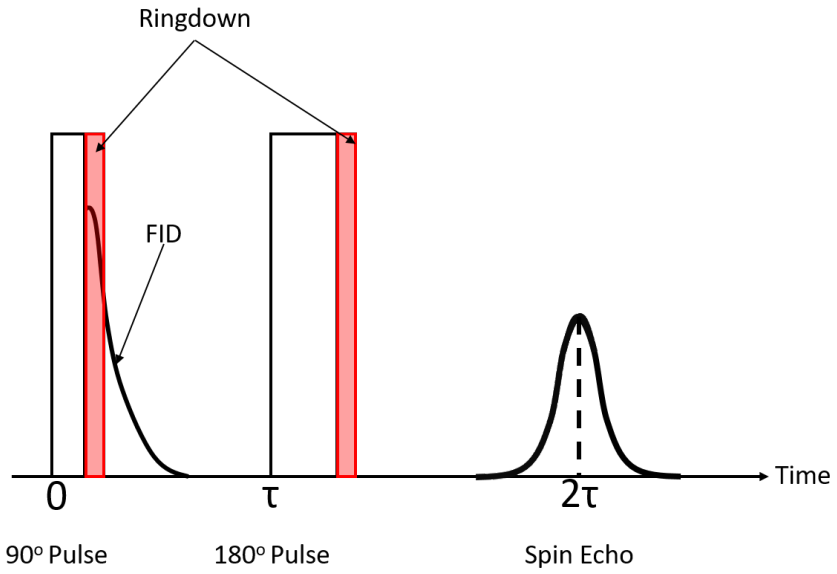

FIGURE 2.2: Spin echo pulse sequence. It should be noted that the pulses contain the desired NMR RF within the pulse width.

The lineshape and NMR frequency shift experiments in this thesis use a more sophisticated method called a spin echo. This method applies two pulses, a 90° pulse followed by a 180° pulse after time τ. Spin echo pulse sequences are used to minimize problems caused by ringdown. Ringdown is caused by the high voltage radio frequency (RF) pulses persisting in the tuned RLC circuit due to the finite Q value of the circuit. It will usually take upwards of 10μs for the voltage to dissipate, and some of this high voltage will end up in the preamplifiers. The leaked voltage will be overlayed on any FID signal produced, which is problematic if the FID signal only lasts for 10μs. In this case, the ringdown will render the FID signal unuseable. The spin echo pulse sequence rectifies this problem as can be seen in figure 2.2. Since the spin echo occurs time τ after the second pulse, much of the ringdown will have been eliminated by the time the spin echo is produced.

Additionally, phase cycling destructively adds ringdown, but constructively adds the spin echo signal, further enhancing the signal to noise ratio. Specific selection of phases for both the 90° and 180° pulses eliminates the ringdown, but keeps the spin echo signal.

The spin echo pulse sequence also eliminates effects from the inhomogeneity of the field, which results in spins precessing at different rates at different spatial points in the sample. Refer to figure 2.2 to see the pulse sequence and figure 2.3 for explanation of how this eliminates some dephasing.

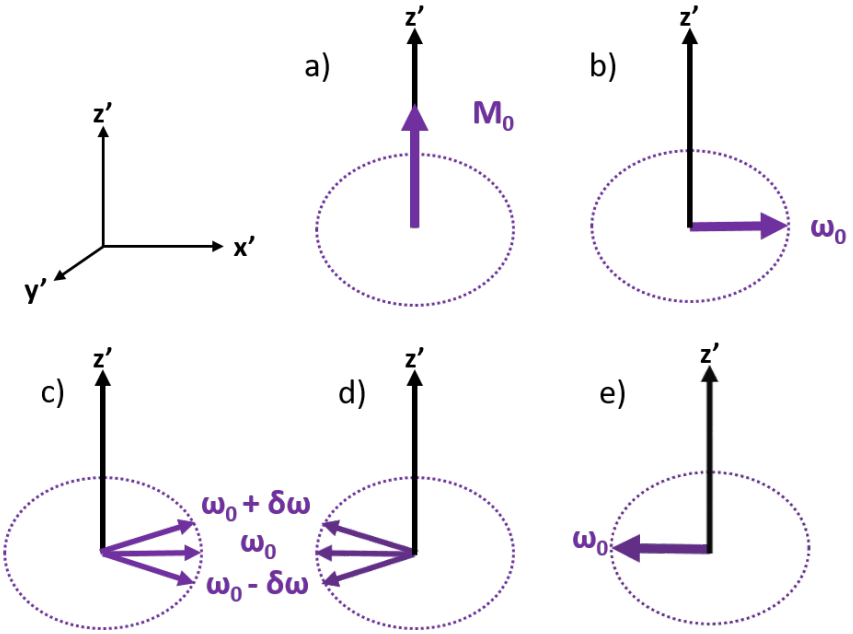

FIGURE 2.3: The spin echo procedure as viewed from a nuclear spin in the rotational frame (at ω_0 about the z axis). a) Nuclear spins initially point along the z' axis. b)The 90° pulse is applied to flip the spin into the y' direction. c) dephasing occurs and the spins "fan out". d) the 180° pulse is applied, mirroring the spins about the y-z plane. e) spin echo is seen when spins realign in the negative x' direction.

2.3 NMR Electronics

Figure 2.4 shows a schematic diagram of the NMR setup. A computer program called TNMR allows us to vary the pulse sequence parameters. These parameters are sent to the Apollo, which is the control center of the NMR spectrometer. Apollo comes with a built in frequency generator. Once it receives commands from the computer, it creates the desired pulse sequence which is amplified by about 60dB by the power amplifier. The back to back diodes following the power amplifier are arranged to ensure only RF pulses of high enough voltage are allowed through to the NMR probe. This eliminates white noise that may have been amplified by the power amplifier.

The amplified pulse sequence then goes to the NMR probe which consists of an LC circuit with two variable capacitors in parallel. The resonance frequency of this LC circuit goes as $\omega_0 \approxeq \frac{1}{\sqrt{L(C_m+C_t)}}$ with L the inductance of the solenoid (coil containing sample), C_m the matching capacitance and C_t the tuning capacitance. Varying C_t tunes the NMR probe resonant frequency to the incoming frequency of the pulse sequence. If this is not done, the high voltage pulses will be reflected and potentially damage the

power amplifier. C_m is used to match the impedance of the LC circuit to 50 Ω and is often quite small (on the order of picofarads). Impedance matching ensures that the maximum amount of power will travel from the amplifier to the LC circuit in the probe.

The pulse sequence goes into the coil and generates an NMR signal from the sample as described previously. This signal goes into the RF preamplifier box. The $\lambda/4$ cable is 1/4 of the wavelength of the amplified RF pulse and is there to short out the high voltage RF pulses from the power amplifier as it creates a standing wave with a node at the end. This allows the NMR signal to go to the preamplifiers without being overwhelmed by the high voltage pulses. The NMR signal then goes from the preamplifiers to the Apollo where the signal is digitized, amplified digitally, recorded and then sent to the computer.

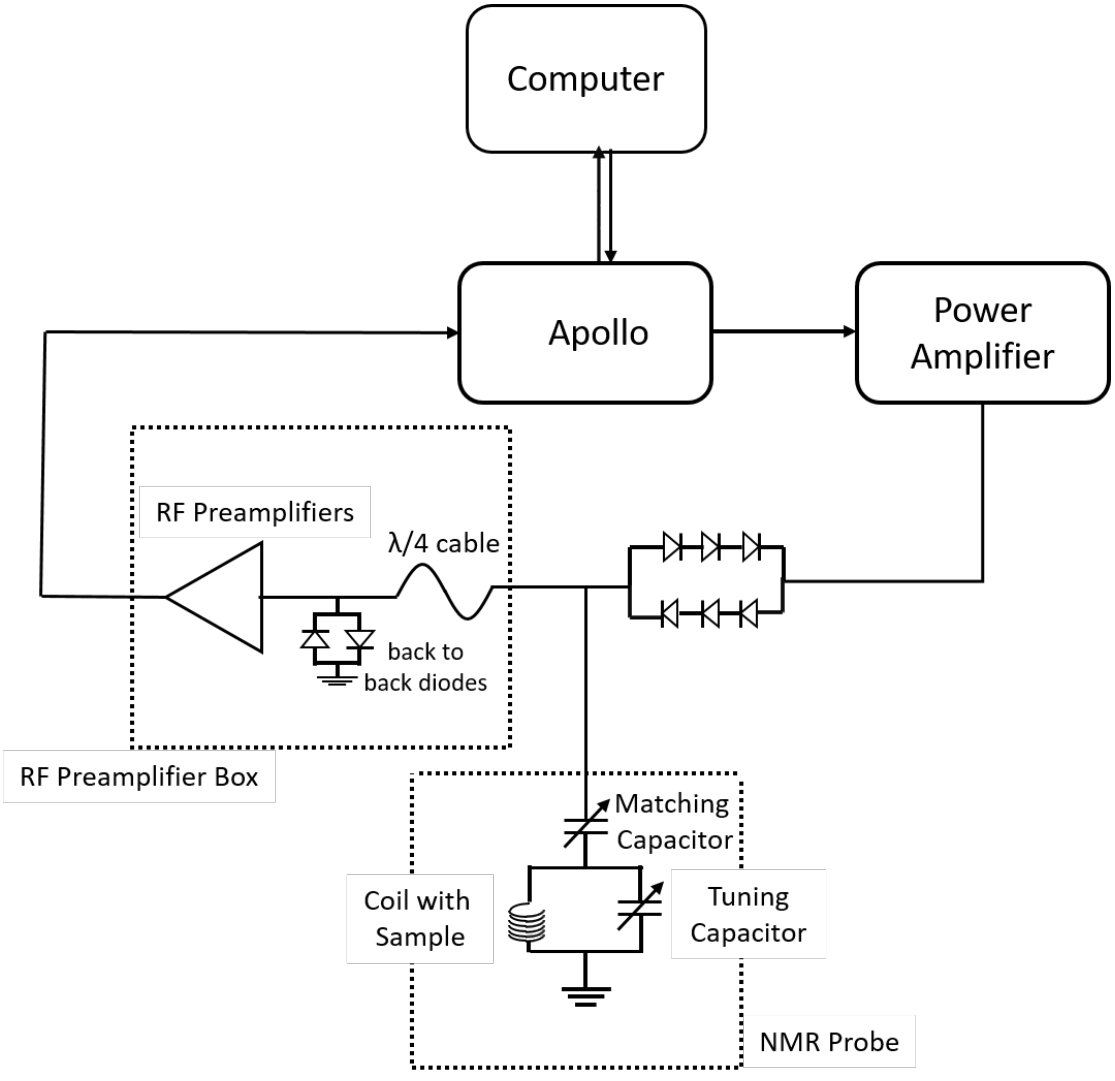

FIGURE 2.4: Schematic diagram of NMR electronic setup.

2.4 The NMR Frequency Shift

In the most general sense, the NMR frequency shift represents how different the local field at a nuclear site is from the applied field. It measures the static susceptibility at the nuclear site. The NMR frequency shift a.k.a. the Knight shift modifies the resonance condition from $f_0 = \frac{\gamma_N}{2\pi}\boldsymbol{B_0}$ to

$$f = \frac{\gamma_N}{2\pi}\boldsymbol{B_0}(1+K), \tag{2.10}$$

where K is the Knight shift. The spin contribution to the Knight shift is proportional to the static electron spin susceptibility at $\boldsymbol{q} = 0$, $\chi'(q=0)_{spin}$.

There are other terms involved with the Knight shift but can be shown to be temperature independent, meaning they simply act as a constant background. There is an electron orbital component, which is also known as Van Vleck paramagnetism. Second order perturbation theory is used to estimate the effect of the orbital susceptibility and is found to be the following [49]

$$\chi_{orb} = \frac{2\mu_B^2 N}{V}\sum_{\boldsymbol{n}}\frac{|\langle 0|(\boldsymbol{L}_z + g_0\boldsymbol{S}_z|n\rangle|^2}{E_n - E_0}. \tag{2.11}$$

In most cases, χ_{orb} may be considered effectively temperature independent as long as $E_n - E_0$, the energy difference between atomic orbitals is much larger than the temperature ranges our NMR experiments, which take place at less than 300 K.

Additionally, there is a diamagnetic contribution to the susceptibility, χ_{dia}, caused by the inner core electrons response to the applied external field $\boldsymbol{B}_0$. The diamagnetic contribution to the frequency shift in general may be quite small, so it may not affect the frequency shift very much.

Thus, Knight shift can be related to the static electron spin susceptibility

$$K = \frac{A_{hf}}{g\mu_B}\chi'(\boldsymbol{q}=0)_{spin} + K_{orb} + K_{dia}, \tag{2.12}$$

where the term A_{hf} has been introduced as the hyperfine interaction strength between the electrons and the nuclei. K_{orb} and K_{dia} are the orbital and diamagnetic Knight shifts, which will usually be temperature independent in the case of K_{orb} or small in the case of K_{dia}. If this is the case, then the only temperature dependence of the total Knight shift will arise from the first term in equation 2.12.

In order to determine the lineshape and Knight shift for $Yb_2Pt_2O_7$, the integrated spin echo intensity was measured as a function of NMR frequency. This produced a lineshape with a main peak from which the Knight shift could be deduced. Due to the anisotropy of the system, there was also a shoulder which will be discussed in section 2.5.

2.5 NMR Lineshapes

For an isotropic, spin-1/2 powder sample, the NMR lineshape would often take the form resembling a truncated Lorenztian or a Gaussian. For axial symmetric interactions with the NMR nuclei, the resonance frequency may be written as [50].

$$\omega = \omega_0 + \frac{1}{2}\alpha(3\cos^2\theta - 1), \tag{2.13}$$

where θ is the angle between the axial axis and the magnetic field and α is a term which is proportional to the Knight shift. This form assumes exclusively dipolar interactions. We can now define $g(\omega)$ as the intensity of the signal, where $g(\omega)d\omega$ is the number of nuclear spins that are at resonance between ω and $\omega + d\omega$. It is essentially the density of states.

Using this definition of $g(\omega)$ along with equation 2.13 we find an equation for the intensity as a function of frequency.

$$g(\omega) = \frac{1}{\sqrt{3\alpha(2(\omega_0 - \omega) + \alpha)}}, \tag{2.14}$$

with the condition of $\alpha < \omega - \omega_0 < -\frac{1}{2}\alpha$.

It should be noted that $g(\omega)$ diverges when $\omega = \omega_0 - \frac{1}{2}\alpha$ in this form. In actual experiments, sources of broadening such as inhomogeneous broadening (nuclear spins

experience different magnetic fields at different points in space), coupling to the lattice (broadening on the order of $1/T_1$) and broadening due to the spin-spin interactions between nuclei ensure that we do not see the divergence in actual experiments [51]. Figure 2.5 shows the theoretically predicted lineshape and the broadened lineshape.

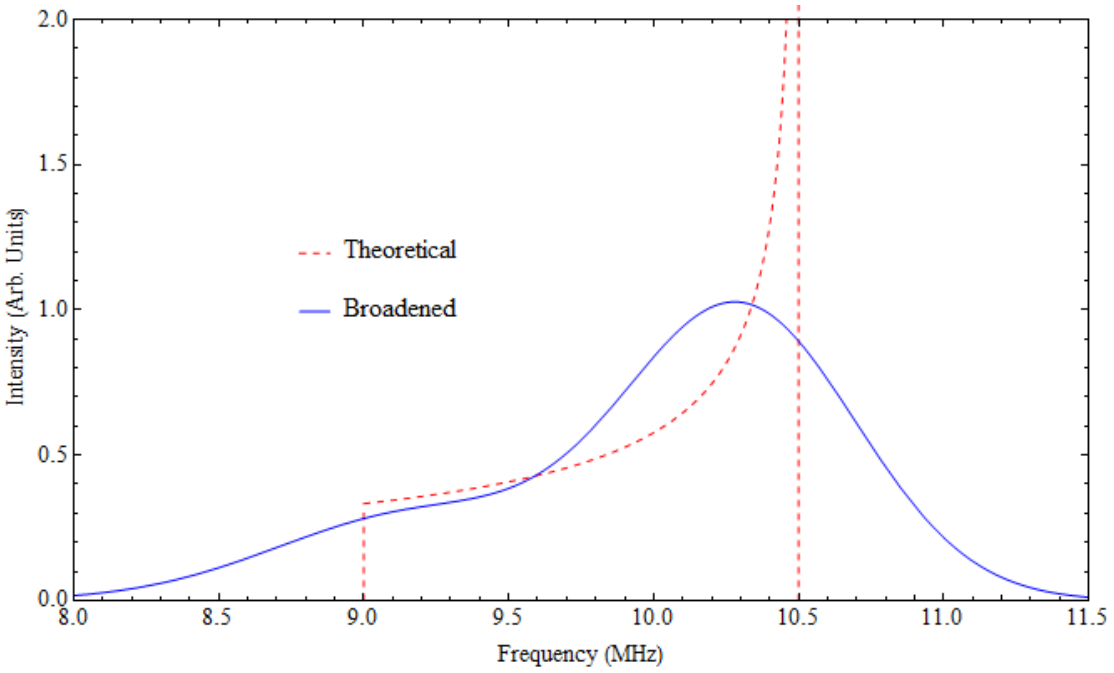

FIGURE 2.5: Theoretically predicted lineshape with divergence with $\omega_0 = 10$MHz, $\alpha = -1$ and broadened lineshape that one may see in an actual experiment.

2.6 Spin-Lattice Relaxation Rate

The spin-lattice relaxation rate, $1/T_1$, is the rate at which the nuclear spins return to thermal equilibrium (nuclear spins pointing along magnetic field) after a perturbation by an RF pulse at resonance frequency. From [52]

$$\frac{1}{T_1} = \frac{\gamma_N^2 \hbar}{2\mu_B^2} \sum_{\boldsymbol{q}} (A_{\perp,1}(\boldsymbol{q})^2 + A_{\perp,2}(\boldsymbol{q})^2) S(\boldsymbol{q}, \omega) \tag{2.15}$$

$A_\perp(\boldsymbol{q})$ is the hyperfine form factor which is perpendicular to the applied magnetic field. $S(\boldsymbol{q}, \omega)$ is the dynamic structure factor which is related to the imaginary part of the dynamic electron spin susceptibility by

$$S(\boldsymbol{q},\omega) = \frac{\chi''(\boldsymbol{q},\omega)}{1-e^{-\hbar\omega\beta}}, \tag{2.16}$$

where β is the usual Boltzmann factor $1/k_{\mathrm{B}}T$. The dynamic structure factor is defined in the following way [53].

$$S(\boldsymbol{q},\omega) = \frac{1}{2\pi}\sum_{\boldsymbol{r}_i}\int_{-\infty}^{\infty}\langle S(0,0)S(\boldsymbol{r}_i,t)\rangle e^{(\boldsymbol{q}\cdot\boldsymbol{r}_i-\omega t)}dt, \tag{2.17}$$

where $\boldsymbol{r}_i$ is the position of the i^{th} electron spin relative to another atom with spin located at $\boldsymbol{r}$ =(0,0). From this form of the dynamic structure factor, it is the space-time Fourier transform of the spin-spin correlation function $\langle S(0,0)S(\boldsymbol{r}_i,t)\rangle$.

Since NMR is a low frequency probe we can approximate equation 2.16 from [54]

$$S(\boldsymbol{q},\omega_{\mathrm{NMR}}) \propto T\frac{\chi''(\boldsymbol{q},\omega_{\mathrm{NMR}})}{\omega_{\mathrm{NMR}}} \tag{2.18}$$

Where ω_{NMR} is the NMR frequency the system is being probed at. Using equation 2.18 along with 2.15 we see that we can find a form for $1/T_1T$.

$$\frac{1}{T_1T} \propto \sum_{\boldsymbol{q}}|A_{\perp}(\boldsymbol{q})|^2\frac{\chi''(\boldsymbol{q},\omega_{\mathrm{NMR}})}{\omega_{\mathrm{NMR}}} \tag{2.19}$$

Where the hyperfine form factors in equation 2.15 have been condensed for the sake of notation. A simple explanation of $1/T_1T$ is that it measures the magnitude of the low frequency spin fluctuations perpendicular to the quantization axis of the observed nuclear spin, which is generally in the direction of the applied field in high field NMR experiments.

T_1 measurements are similar to the spin echo measurements, except that a 180° inversion pulse is applied before the spin echo sequence. The pulse sequence is shown in figure 2.6. The inverted spins are allowed to relax for time called the long delay time (LD) before the spin echo sequence measures the NMR signal. The longer the spins are allowed to relax, the closer they get back to their equilibrium position. For example, there will be a time LD_0 such that there will be no NMR signal as the spins will have relaxed into the

x-y plane. Thus, a spin echo pulse sequence would flip them into the -z direction, then to the +z direction, which will not allow for any precession about the magnetic field direction. If the spin echo pulse sequence was applied immediately after the inversion $LD = 0$, the NMR signal intensity will be equal and opposite to if all the spins were allowed to relax to equilibrium $LD \to \infty$. LD is varied and follows and can be fit to an exponential relaxation curve to determine T_1.

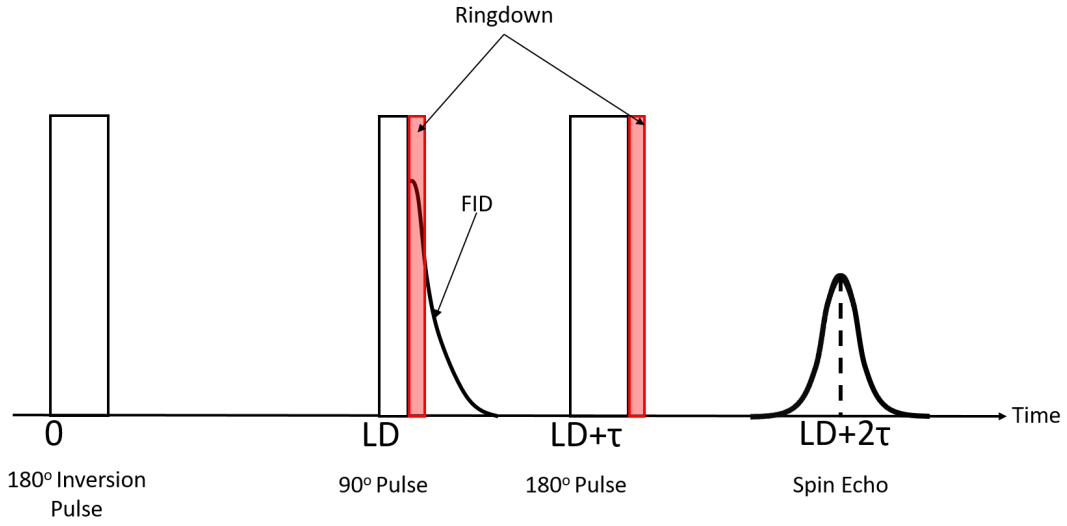

FIGURE 2.6: Pulse sequence used to determine $1/T_1$.

Chapter 3

Results

3.1 Lineshape

We conducted lineshape measurements using the spin echo method and integrating over the spin echo intensity. In figure 3.1 below, we present representative lineshapes observed at 2 T applied field at temperatures 5K, 30K and 63K. We normalized the integrated intensity with respect to temperature using the Boltzmann factor $\propto e^{-hf/k_BT} \sim 1/T$. The lineshape broadens dramatically at low temperatures. As can be seen from figure 3.1, the lineshape is assymetrical where there is a main peak and a shoulder. This is analogous to the axially symmetric case with dipolar coupling as discussed in chapter 2.

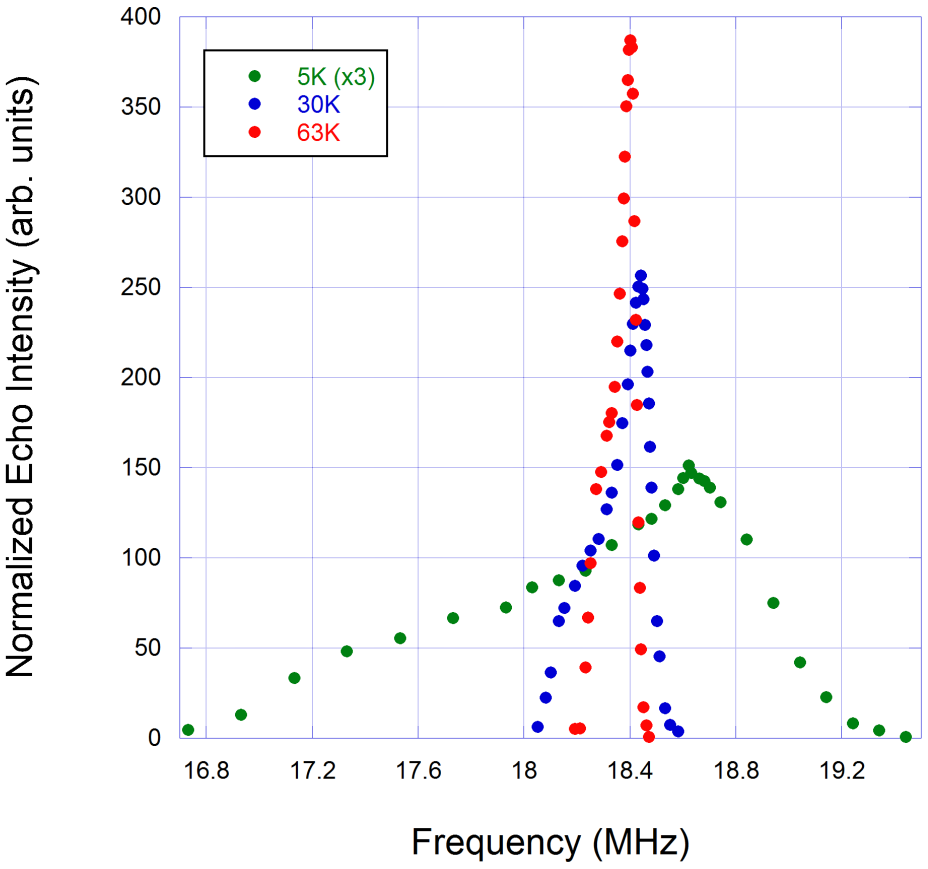

FIGURE 3.1: Normalized lineshape measurements at 2 T with varying temperature. The lineshape at 5 K has been multiplied by 3 so that its features can be observed on the same level as higher temperatures.

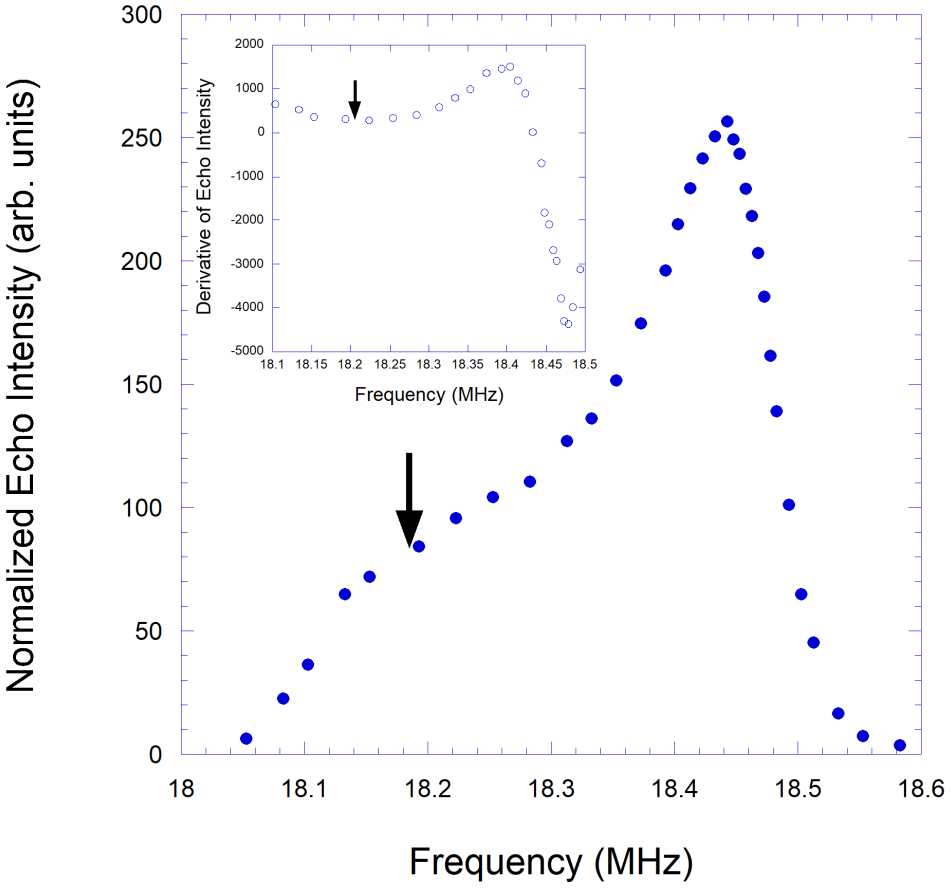

FIGURE 3.2: The main figure is the normalized lineshape at 2 T at 30 K. The inset is the first derivative of the lineshape. The black arrow shows where the shoulder is defined.

The position of the main peak at 18.44 MHz was found simply by fitting a Gaussian to the peak region and extracting the peak from the fit. This method was followed cautiously at low temperatures with the broadened line, as including/excluding one or two fringe points could change the position of the peak by ~ 0.03 MHz, which translates to about 0.3% in frequency shift at 1 T. This is what contributes to the large errors at low temperatures as seen in the next section.

Figure 3.2 above gives an example of how the shoulder was defined for each lineshape. The first derivative of the lineshape was taken. The point at which there was a local

minimum in the2 first derivative describes an inflection point. This inflection point was used to define the position of the shoulder. This was obviously an increasingly difficult task as the lineshape broadened, which is why the errors at lower temperatures are so much larger than at higher temperatures in the next section.

3.2 Frequency Shift and Susceptibility

We summarize the NMR frequency shift of the main peak $^{195}K_{\text{main}}$ in figure 3.3. As can be seen, $^{195}K_{\text{main}}$ increased as temperature was decreased. In contrast, the frequency shift of the shoulder $^{195}K_{\text{shoulder}}$ displayed the opposite behaviour and decreased to lower frequencies with decreasing temperature as seen in figure 3.4. The anisotropic magnitude of the frequency shifts is related to the anisotropy of the Yb^{3+} moment polarization in the XY plane and the shoulder is related to the Yb^{3+} moment in the z-direction.

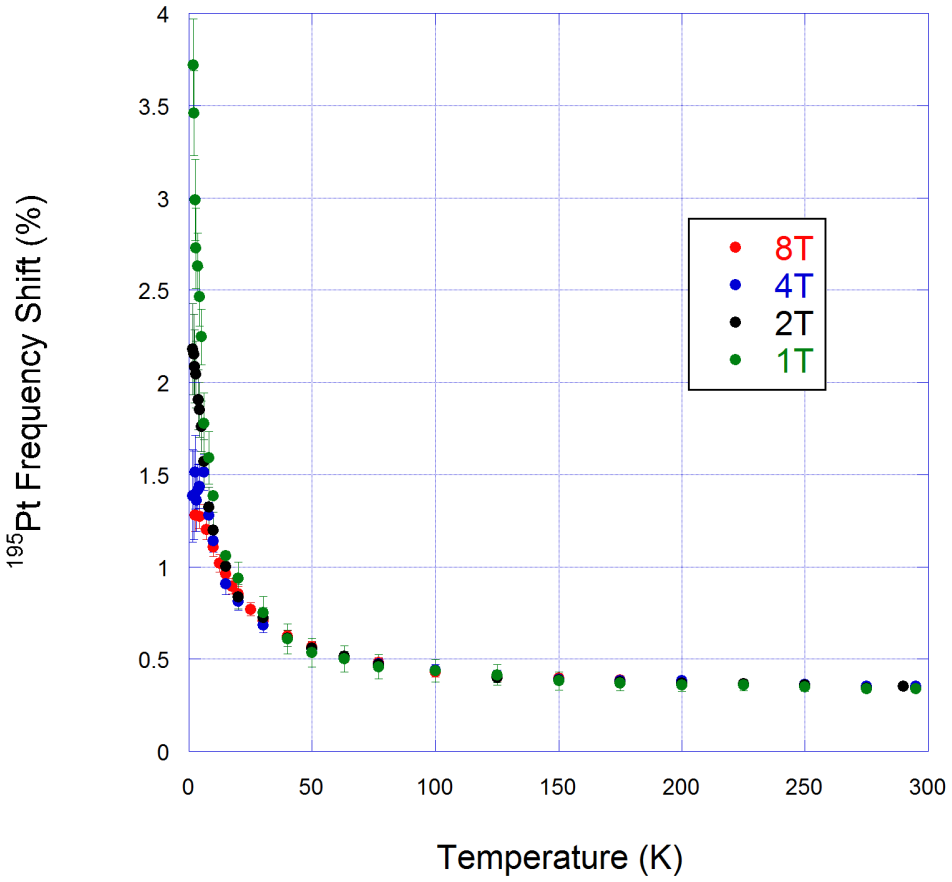

FIGURE 3.3: $^{195}K_{\text{main}}$ for different fields. The frequency shift begins to level off for higher fields at low temperature.

In 8 T, 4 T and 2 T $^{195}K_{\text{main}}$ saturated in the lowest temperature range because of the strength of the magnetic field. In high magnetic fields, a complete spin polarization can be achieved which in turn saturates the internal fields seen by the nuclei. The saturation of the internal fields causes the frequency shift to become saturated below a certain temperature as well. This did not occur at the lower 1T field. The reason that $^{195}K_{\text{shoulder}}$ was not found for temperatures above 200K was that it became too difficult to decipher the shoulder from the main peak. At this high temperature region, the frequency shift of the main peak and the shoulder converge to each other within experimental resolution.

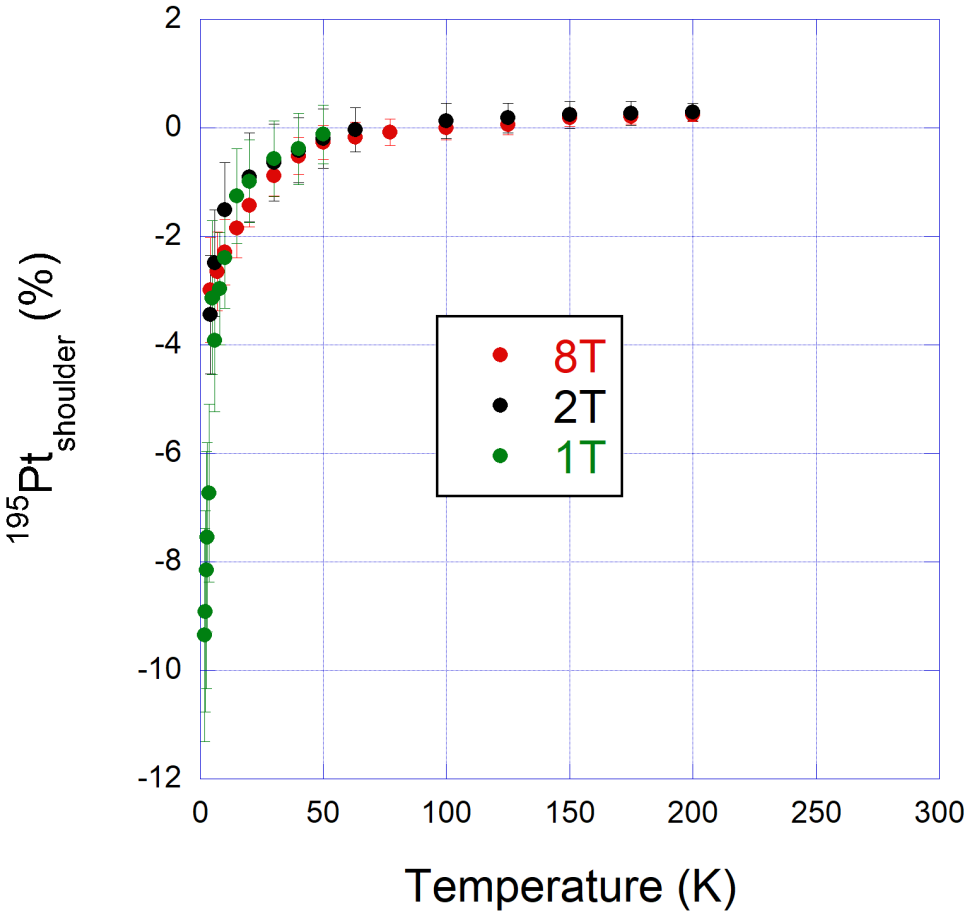

FIGURE 3.4: $^{195}K_{\text{shoulder}}$ as a function of temperature. There is no shoulder data for 4 T because the shoulder was cut off due to the probe not being able to be tuned to those frequencies. There are error bars at high temperatures, but the are very small because the shoulder was relatively narrow so easy to distinguish.

Using the idea that the frequency shift of the shoulder $^{195}K_{shoulder}$ corresponds to the parallel component of the frequency shift, $^{195}K_{\text{main}}$ corresponds to the perpendicular. We can then we can define $K_{Shoulder} = K_{\parallel}$ and $K_{main} = K_{\perp}$. From this, the isotropic frequency shift is $K_{iso} = \frac{1}{3}(2K_{\perp} + K_{\parallel})$. This is plotted in figure 3.5 below. It closely resembles the frequency shift of the shoulder. One surprise is that the 2T data does not seem to diverge any faster than the 8T data, however, the error here is relatively large. K_{iso} does decrease quickly in the 1 T case.

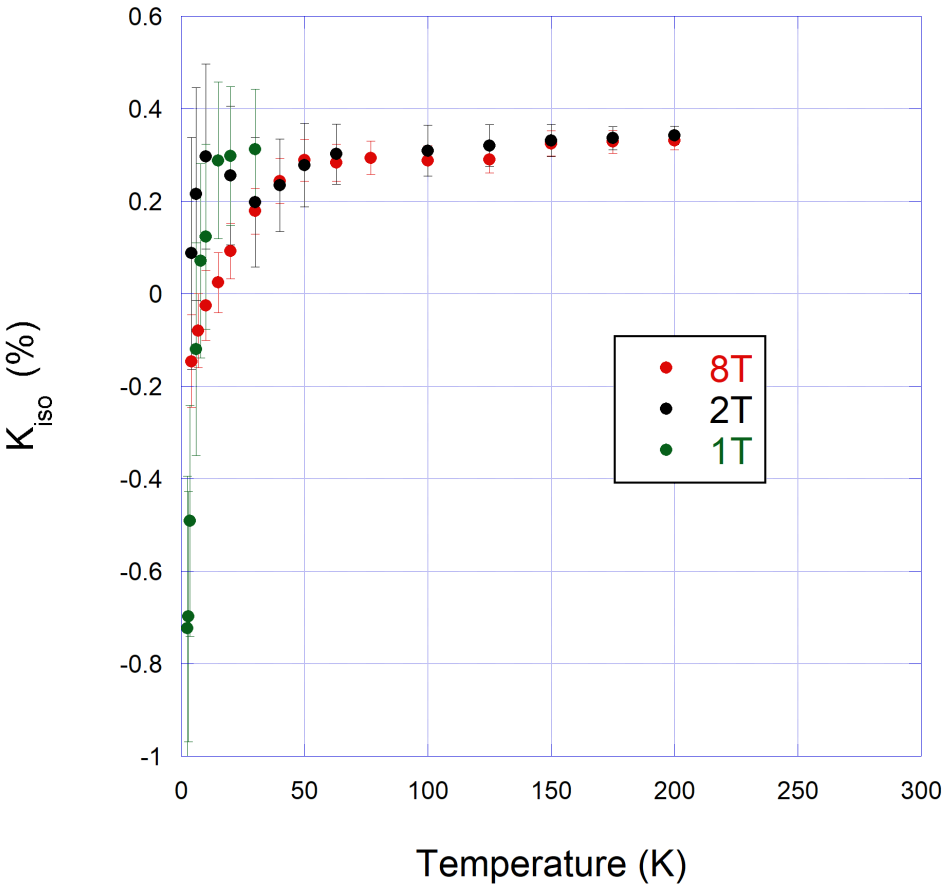

FIGURE 3.5: Isotropic frequency shift as a function of temperature. The isotropic shift is defined by $K_{iso} = \frac{1}{3}(2K_{\perp} + K_{\parallel})$.

A DC SQUID was used to determine the molar susceptibility of $Yb_2Pt_2O_7$. The data is shown below in figure 3.6 along with the inverse of the molar susceptibility. This data was compared to previously measured values of $Yb_2Pt_2O_7$ from [35], which quantitatively matches very well.

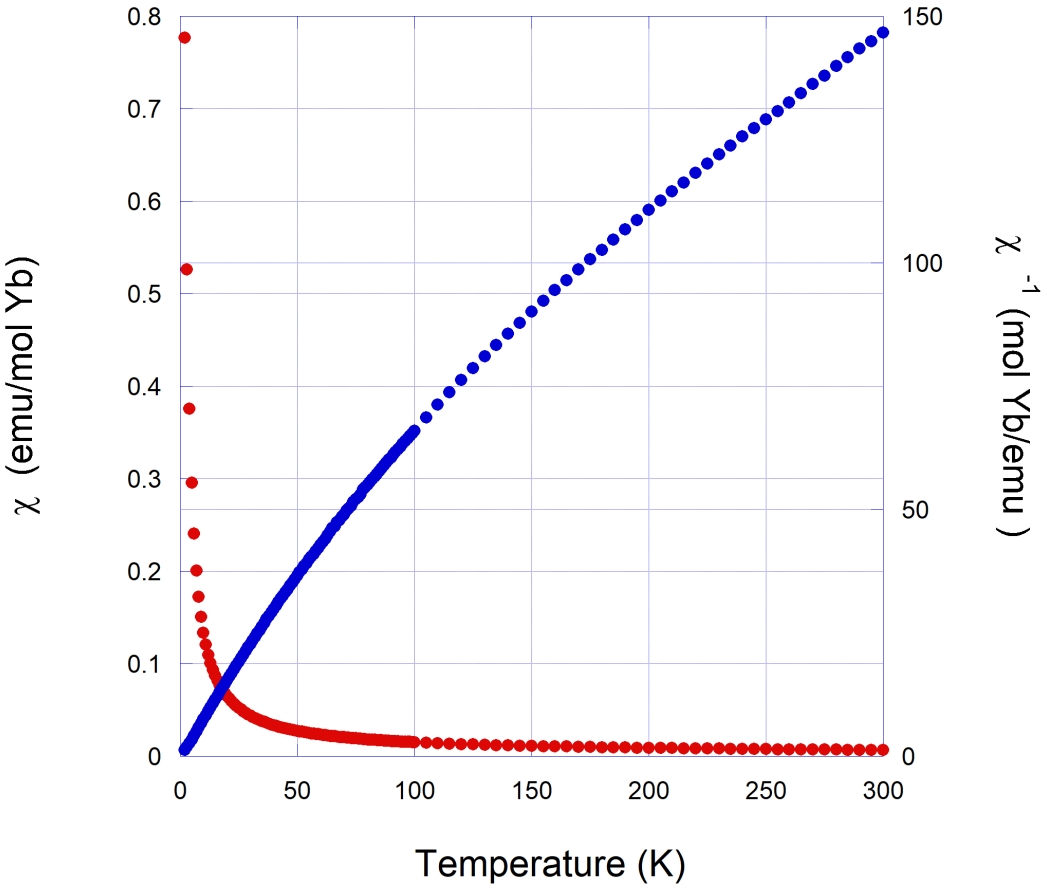

FIGURE 3.6: Susceptibility per mole of ytterbium (red, left axis) and inverse susceptibility (blue, right axis) as a function of temperature. The data was taken at 0.5 T with a DC SQUID.

Figure 3.7 below is a Curie-Weiss fit of the molar susceptibility data as a function of temperature for temperatures in the range of 2-19K. The μ_{eff} obtained from this fit was $3.2 \pm 0.3\mu_B$ which is within range of the value of $3.08\mu_B$ reported in [35]. The transition temperature for $Yb_2Pt_2O_7$ is around 0.3K which means that the Curie-Weiss approximation seems still valid for this region. Cai et al. also reported a bulk of $T_c \sim 0.3$ K while $T_c = 0.64 \pm 0.06$ K from our fit.

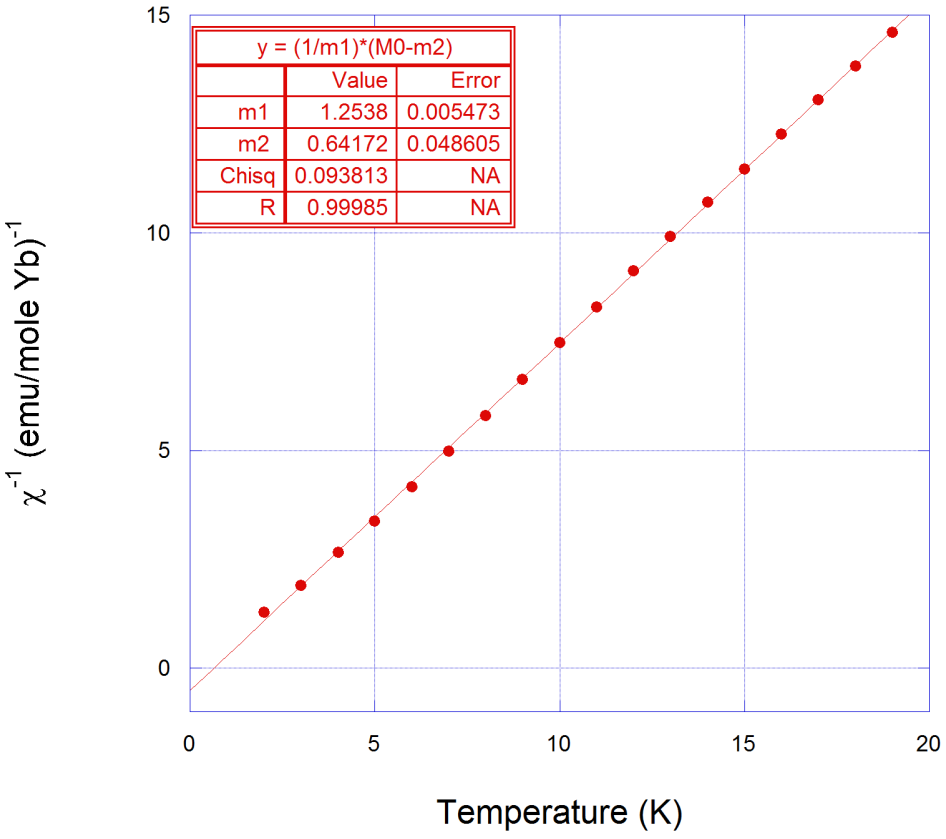

FIGURE 3.7: Curie-Weiss fit of the susceptibility data below 20 K. This gives a Curie temperature of $\theta_{CW} = 0.64 \pm 0.06$ K and $\mu_{eff} = 3.2 \pm 0.3\mu_B$.

Figures 3.8 and 3.9 are plots of $^{195}K_{\text{main}}$ and $^{195}K_{\text{shoulder}}$ versus the magnetic moment per mole of ytterbium for the main peak and shoulder respectively. As mentioned previously, the main peak frequency shift corresponds to the perpendicular direction and the shoulder corresponds to the parallel.

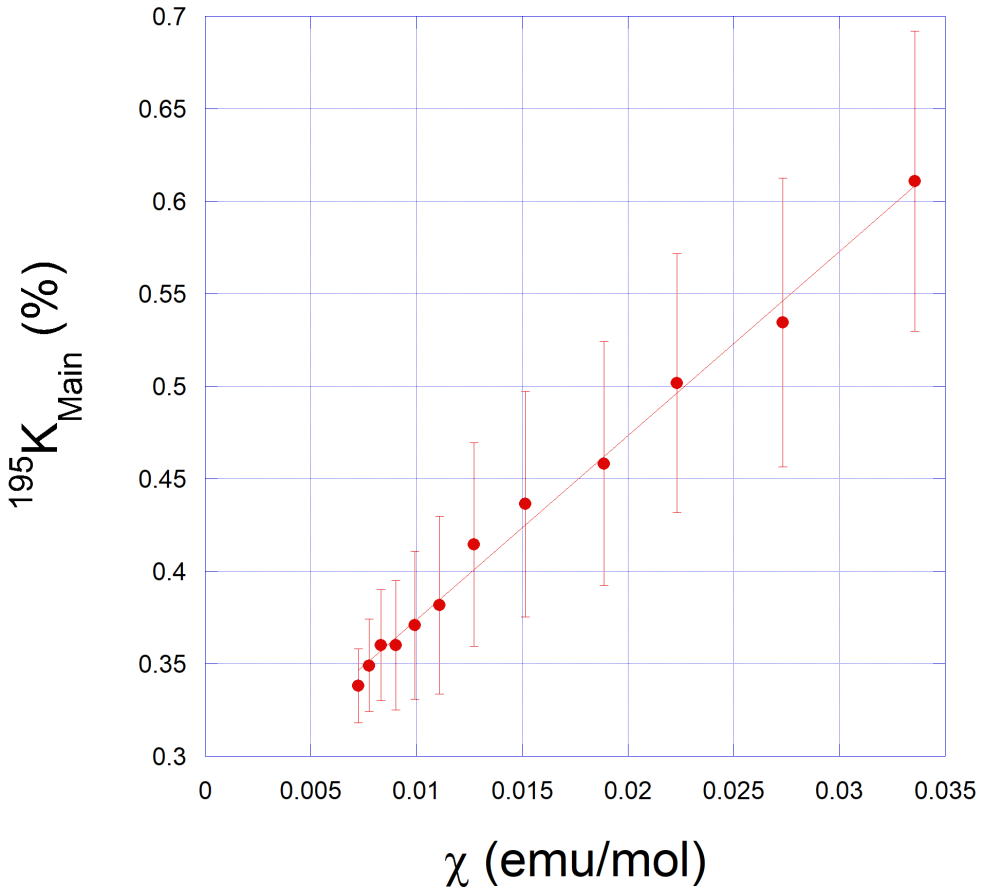

FIGURE 3.8: The frequency shift of the main peak as a function of the susceptibility per mole of ytterbium. The straight line represents the best fit.

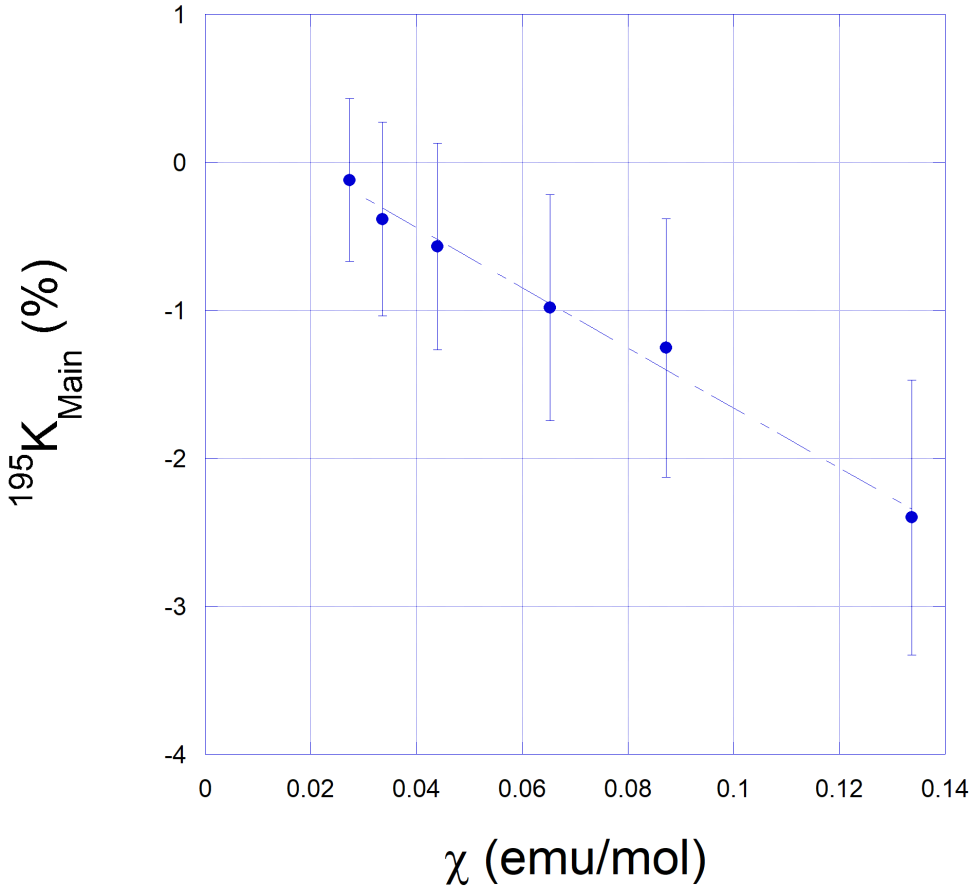

FIGURE 3.9: The frequency shift of the shoulder as a function of the susceptibility per mole of ytterbium at 1 T. The straight line represents the best fit.

$^{195}K_{\text{main}}$ increases linearly with magnetic moment, whereas the shoulder shows opposite behaviour. From the K-χ plots we can deduce the hyperfine field constants $A_{hf\perp}$ and $A_{hf\parallel}$. This is done by taking the slope of the line of best fit and multiplying by $N_A\mu_B$. The results for the main peak are plotted as a function of field below.

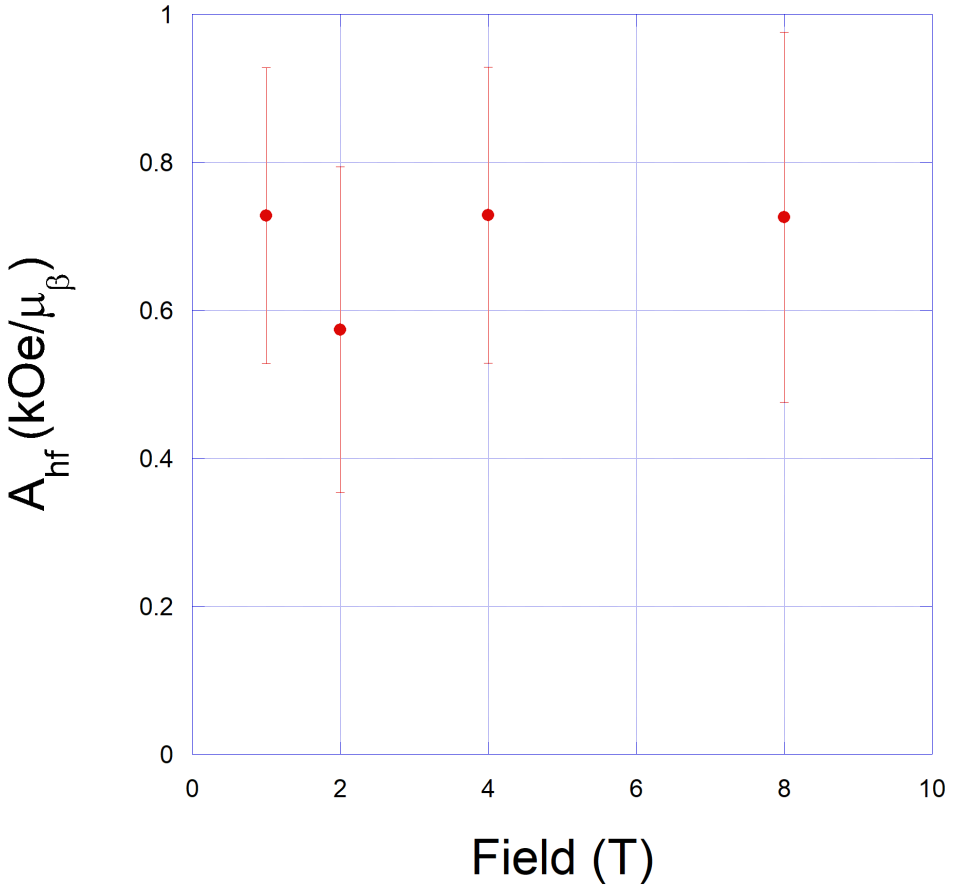

FIGURE 3.10: The experimental $A_{hf\perp}$ as a function of field.

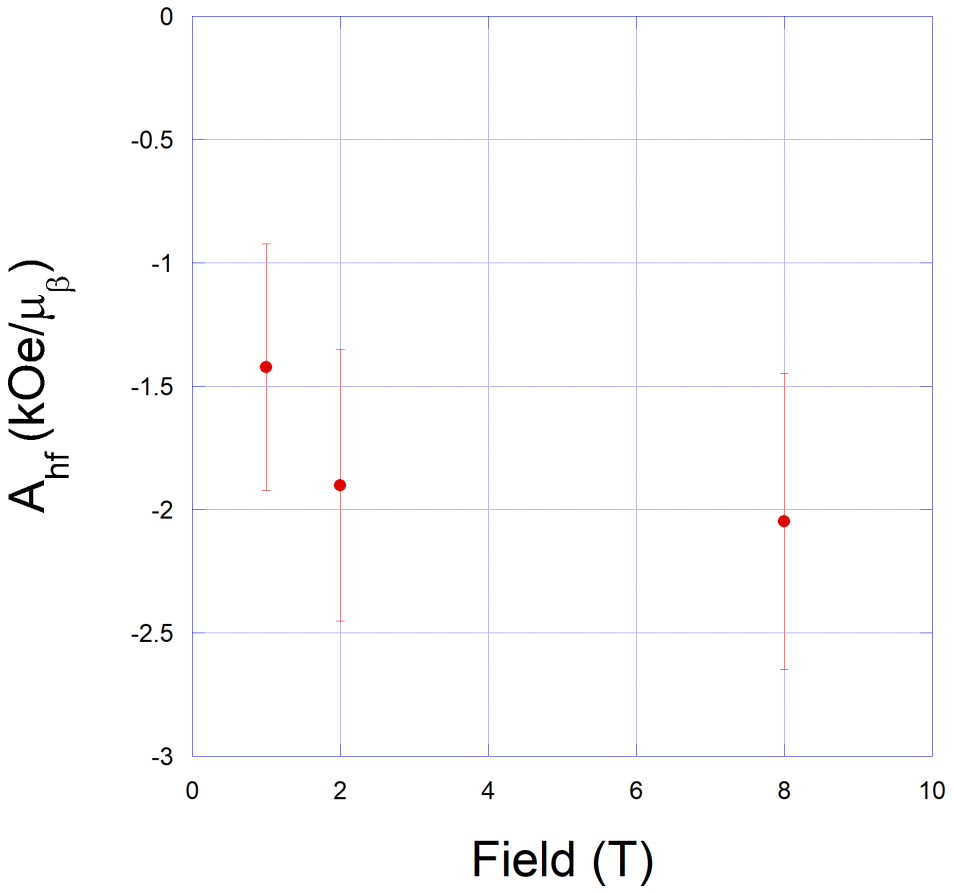

FIGURE 3.11: The experimental $A_{hf\parallel}$ as a function of field.

From figure 3.10, it appears that $A_{hf\perp}$ is relatively constant with field as it should be. It appears that $A_{hf\parallel}$ has deviation at 1T as seen in figure 3.11, however this is still within error of the 2 T and 8 T data.

3.3 T_1 Measurements

As explained in chapter 2, the long delay (LD) of a $1/T_1$ measurement is the time between inverting the nuclear spins to align in the negative direction of the applied field and the spin echo sequence that probes the net magnetization. This is plotted along the x-axis and the integrated intensity of the spin echo is plotted along the y-axis. This can

be fit to an exponential recovery curve to determine $1/T_1$ where it is a fit parameter. A sample set of data along with the corresponding fit curve is shown in figure 3.12.

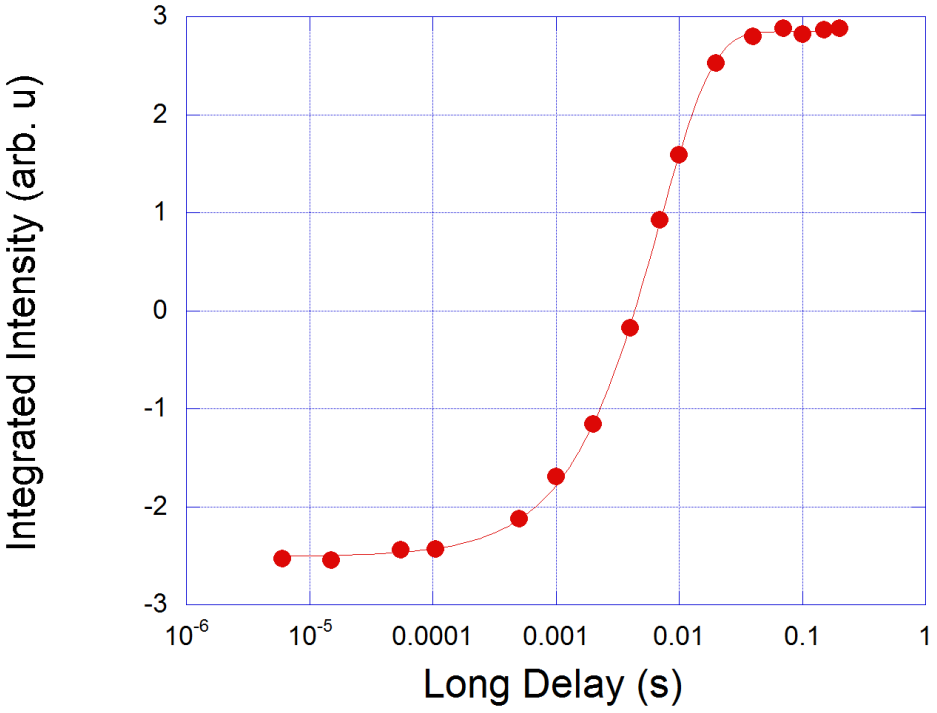

FIGURE 3.12: Example of a T_1 measurement at 4.2 K in 2 T external field. The data is fit to $y = A - Be^{-LD \times \frac{1}{T_1}}$ where y is the integrated echo intensity, A, B and T_1 are the fit parameters and LD is the long delay. The solid line is the curve fit to the data points.

The temperature dependence of $1/T_1$ was qualitatively similar for all magnetic fields. There was a broad peak between 50 K and 100 K, then $1/T_1$ began to slowly decrease with decreasing temperature. Below about 15 K, exponential behaviour clearly began developing for the three higher fields. $1/T_1$ still decreased rapidly with temperature at 1T, but it is debatable about whether the behaviour is exponential. Refer to figure 3.13 for data.

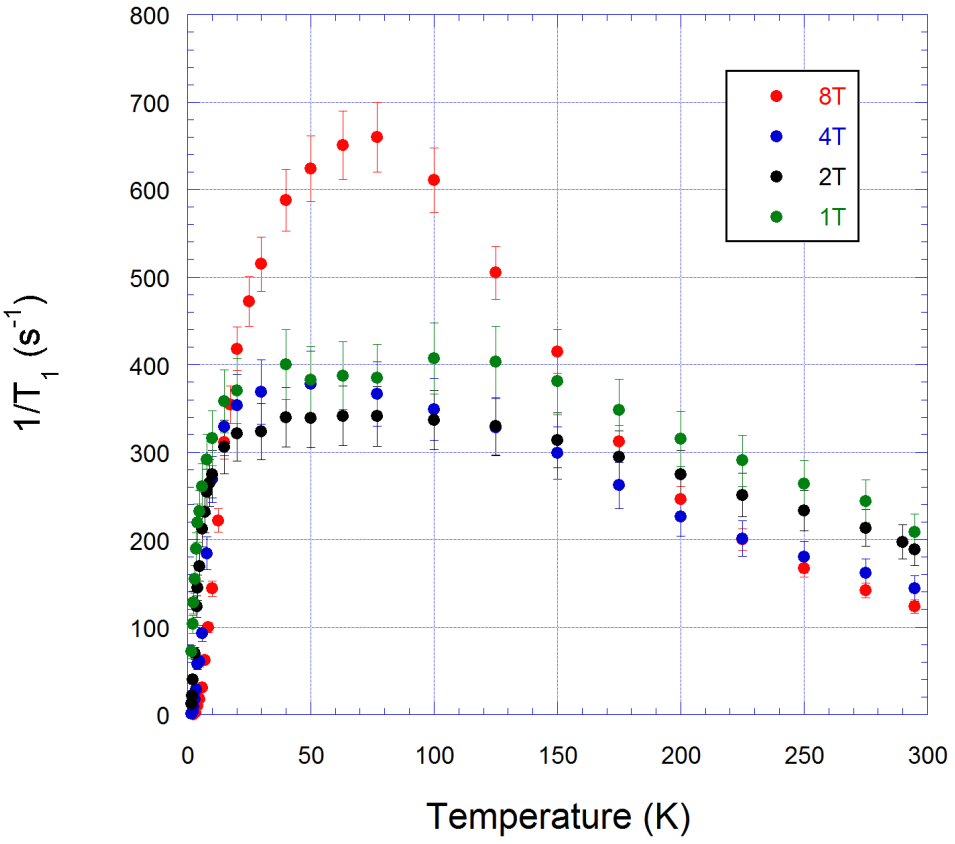

FIGURE 3.13: $1/T_1$ measurements as a function of temperature for the different fields. In all 4 field strengths, $1/T_1$ begins to quickly diminish at low temperatures.

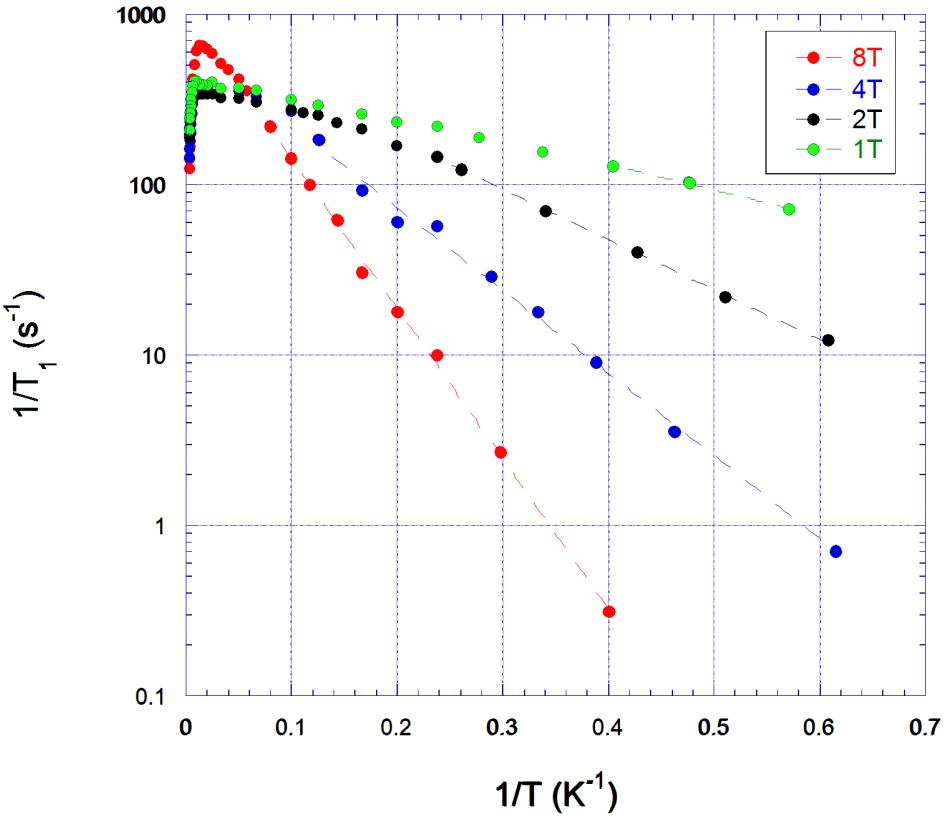

FIGURE 3.14: $1/T_1$ as a function of inverse temperature, plotted on a semi-logarithmic plot. This shows the exponential behaviour of $1/T_1$ at lower temperatures. The $1/T_1$ data was fit to an exponential of the form $e^{-\Delta/T}$ where Δ is a fit parameter and represents an energy scale. The dashed lines represent the fit curve.

Figure 3.14 above shows $1/T_1$ measurements as a function of inverse temperature 1/T. At 8 T, 4 T and 2 T, we clearly observe exponential behaviour, which suggests a field-induced gap. At 1 T, the exponential behaviour is less clear. Qualitatively, the same behaviour exists at 1T when compared to the higher fields, but the reduction of $1/T_1$ in the low temperature regime is not nearly as extreme. This brings up the question of whether or not there is a gap. This data was fit to $e^{-\Delta/T}$ in order to determine the fit parameter Δ. This is an energy scale associated with the system. The fits are shown in figure 3.14.

3.4 Energy Scale

As mentioned in the previous section, one method of defining an energy scale with the system is by fitting the $1/T_1$ vs $1/T$ plot with an exponential and defining the energy scale as the fit parameter Δ. This method is somewhat crude as there are limited data points that show exponential behaviour at the two lower fields.

Determining the peak of a $1/T_1T$ vs temperature plot also displays an energy scale. Since $1/T_1T$ essentially measures the spin fluctuations perpendicular to the magnetization axis, the position of the peak corresponds to the temperature where these fluctuations are maximal. One can also note from figure 3.15 that the fluctuations clearly die out at 2 T, 4 T and 8 T although the temperature range of our measurements is not low enough at 2 T. Lower temperature measurements are necessary to determine if the fluctuations also die out at 1 T. The advantage of this method over the previous is that the peaks can be clearly seen at all field values. Even though the 8 T peak is quite broad, it still clearly follows the trend that the peak moves to higher temperatures with higher fields.

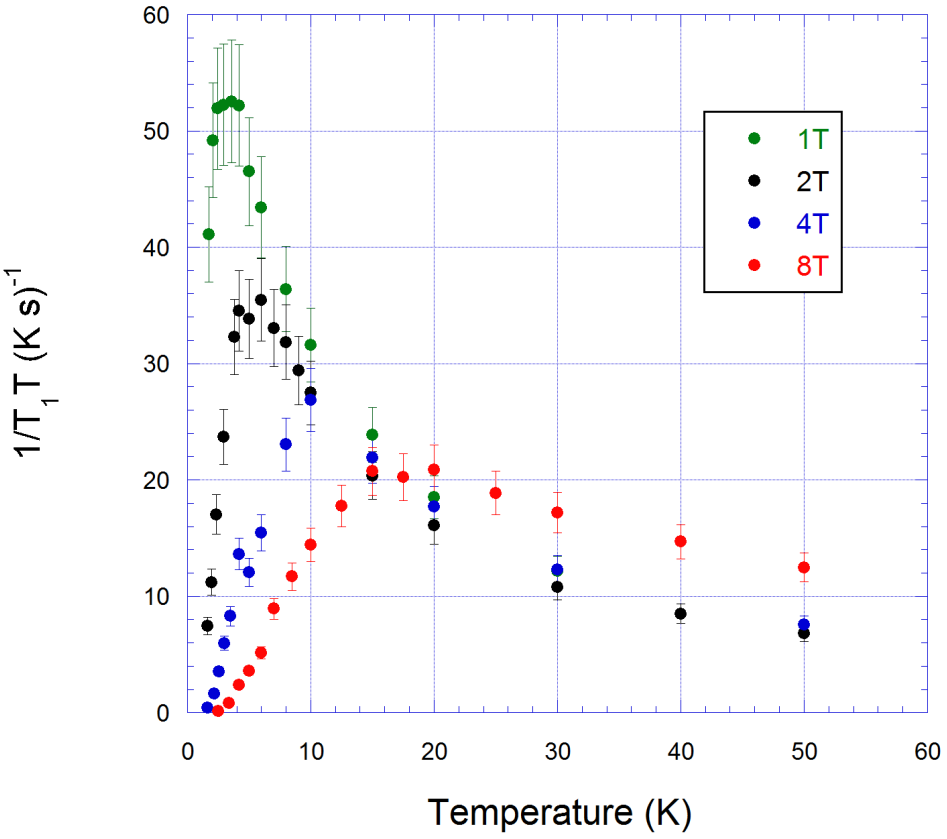

FIGURE 3.15: $1/T_1T$ as a function of temperature. The energy scale Δ can be estimated by the peak of the plot for each field.

A third way of estimating the energy scale is through scaling analysis. This was done using a modified $1/T_1$ vs $1/T$ plot. For each of the four sets of data, $1/T_1$ was multiplied by a constant so that all of them were normalized to the same height. Then, $1/T$ was multiplied by a constant Δ, which again represents the energy scale. Δ/T was modified for each of the four of the data sets until they were overlayed on top of each other as shown in figure 3.16. The results of scaling analysis also showed that Δ is linear with magnetic field strength.

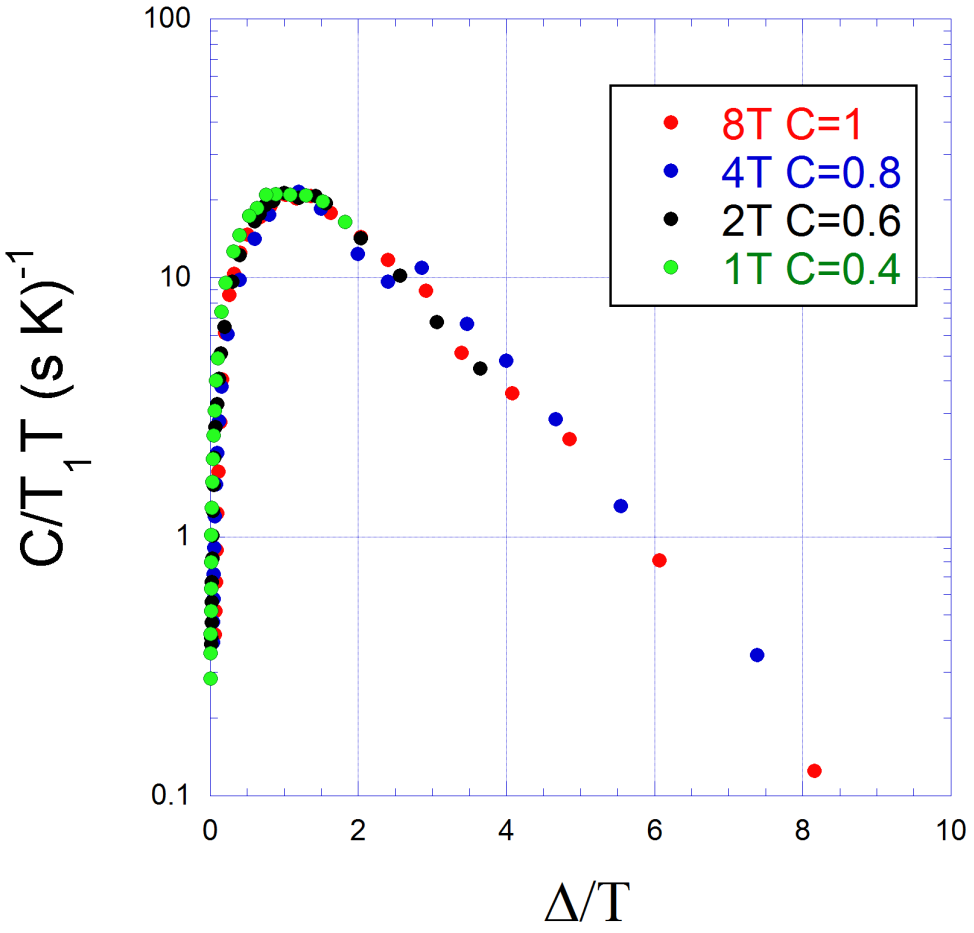

FIGURE 3.16: Modified $\mathrm{Log}(1/T_1T)$ vs $1/T$ plot. Before modification, the peaks for the different fields were different heights and in different positions. After modification, the data from each field lies over each other. The constant multipying the 8T data set was set at 1 and the lower fields data sets were multiplied by 0.8, 0.6 and 0.4 for 4 T, 2 T and 1 T respectively so that all four data sets lined up properly. Δ was then varied for the three lower fields until they all lined up with the 8 T data.

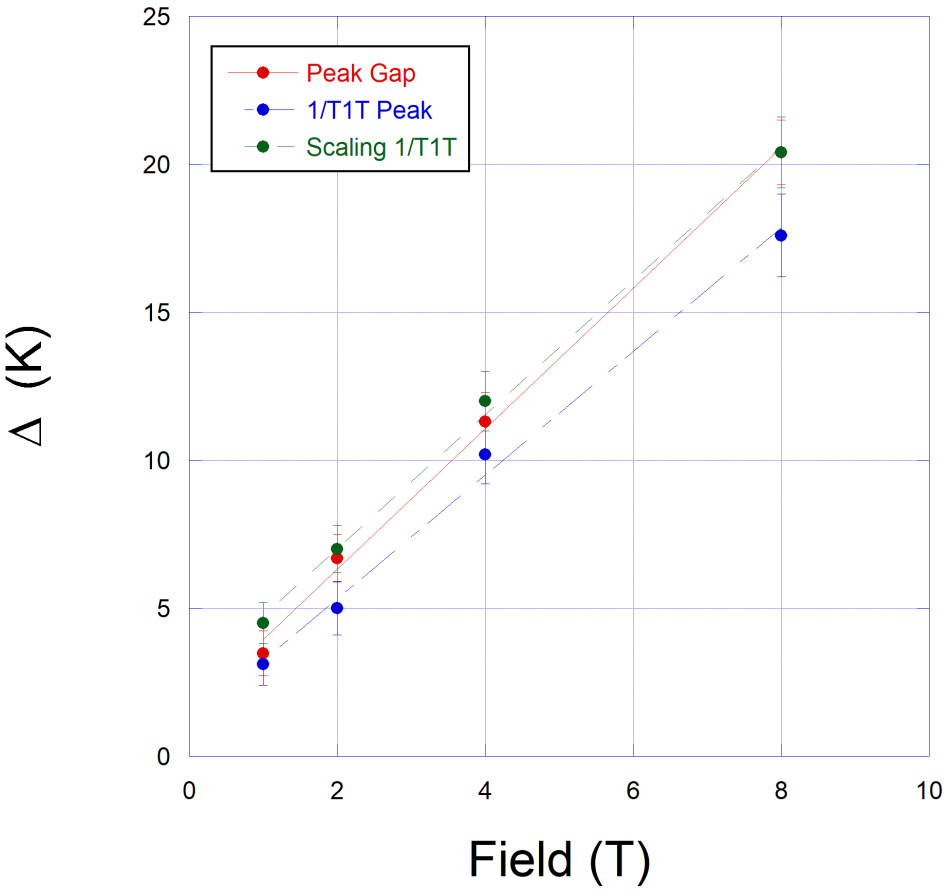

FIGURE 3.17: All the methods used to analyze the behaviour of Δ showed that it goes linearly with magnetic field down to 1 T. The lines show the associated line of best fit for each set of points.

Figure 3.17 above shows that down to 1 T, Δ behaves linearly with temperature. This is consistent with the peak of the broad specific heat anomaly seen in previous experiments (figure 1.9 [47]), which suggests that the spin fluctuations may be influencing the specific heat.

Lower field measurements must be completed to determine the behaviour of Δ in the crucial low field region.

Chapter 4

Conclusion

4.1 Summary

High field NMR experiments were conducted on a powder sample of the pyrochlore $Yb_2Pt_2O_7$. The spin fluctuations tended to die out at low temperatures (below ~20 K) as shown by the rapid decrease in $1/T_1$ with temperature. At 2 T and higher, the behaviour of $1/T_1$ with temperature is exponential, which suggests a field-induced gap. All indications are that 1T results are still similar to 2 T and higher, however, it is not definitive. We are unsure about 0.5 T and need to complete further experiments.

Three methods were used to determine an energy scale Δ: exponential fit of $1/T_1$ data, determination of the $1/T_1T$ peak of the data when plotted against temperature, and scaling analysis. All three of the methods showed the energy scale varied linearly with magnetic field, althought this may not be the case in fields below 1 T. However, the high field behaviour of Δ is the same behaviour of the broad specific heat anomaly seen by D'Ortenzio [47] in the sister compound $Yb_2Ti_2O_7$. It is possible that the bulk specific heat and the magnetic spin fluctuations of the Yb^{3+} ions are related.

4.2 Future Work

We are currently working on low field NMR experiments of the $Yb_2Pt_2O_7$. Experiments down to ~0.3 T may be possible with the current equipment, but lower fields will require more specialized equipment such as a new power amplifier with lower frequency range of

operation. In addition, lower temperature measurements would aid in the analysis of the spin fluctuations. In order to complete more definitive experiments, lower temperature measurements may be attempted in the low field cases. With these experiments, it will be easier to determine the relationship between the spin fluctuations of the system, the energy scale Δ and the specific heat anomaly. This will deepen the understanding of the pyrochlores and geometrically frustrated systems.

Bibliography

[1] J. Bardeen and W. H. Brattain. The transistor, a semi-conductor triode. *Phys. Rev.*, 74:230–231, Jul 1948. doi: 10.1103/PhysRev.74.230.

[2] J. Bardeen, L. N. Cooper, and J. R. Schrieffer. Microscopic theory of superconductivity. *Phys. Rev.*, 106:162–164, Apr 1957. doi: 10.1103/PhysRev.106.162. URL `https://link.aps.org/doi/10.1103/PhysRev.106.162`.

[3] Michael E. Fisher. Renormalization group theory: Its basis and formulation in statistical physics. *Rev. Mod. Phys.*, 70:653–681, Apr 1998. doi: 10.1103/RevModPhys.70.653. URL `https://link.aps.org/doi/10.1103/RevModPhys.70.653`.

[4] J. G. Bednorz and K. A. Müller. Possible high t_c superconductivity in the ba-la-cu-o system. *Zeitschrift für Physik B Condensed Matter*, 64(2):189–193, Jun 1986. ISSN 1431-584X. doi: 10.1007/BF01303701. URL `https://doi.org/10.1007/BF01303701`.

[5] J Vannimenus and G Toulouse. Theory of the frustration effect. ii. ising spins on a square lattice. *Journal of Physics C: Solid State Physics*, 10(18):L537, 1977. URL `http://stacks.iop.org/0022-3719/10/i=18/a=008`.

[6] P.W. Anderson. Resonating valence bonds: A new kind of insulator? *Materials Research Bulletin*, 8(2):153 – 160, 1973. ISSN 0025-5408. doi: http://dx.doi.org/10.1016/0025-5408(73)90167-0. URL `http://www.sciencedirect.com/science/article/pii/0025540873901670`.

[7] G. Baskaran, Z. Zou, and P.W. Anderson. The resonating valence bond state and high-tc superconductivity — a mean field theory. *Solid State Communications*, 63(11):973 – 976, 1987. ISSN 0038-1098. doi: http://dx.doi.org/10.1016/

0038-1098(87)90642-9. URL http://www.sciencedirect.com/science/article/pii/0038109887906429.

[8] M.A. Subramanian, G. Aravamudan, and G.V. Subba Rao. Oxide pyrochlores , a review. *Progress in Solid State Chemistry*, 15(2):55 – 143, 1983. ISSN 0079-6786. doi: http://dx.doi.org/10.1016/0079-6786(83)90001-8. URL http://www.sciencedirect.com/science/article/pii/0079678683900018.

[9] A P Ramirez. Strongly geometrically frustrated magnets. *Annual Review of Materials Science*, 24(1):453–480, 1994. doi: 10.1146/annurev.ms.24.080194.002321. URL https://doi.org/10.1146/annurev.ms.24.080194.002321.

[10] M. J. Harris, S. T. Bramwell, D. F. McMorrow, T. Zeiske, and K. W. Godfrey. Geometrical frustration in the ferromagnetic pyrochlore $ho_2ti_2O_7$. *Phys. Rev. Lett.*, 79:2554–2557, Sep 1997. doi: 10.1103/PhysRevLett.79.2554. URL https://link.aps.org/doi/10.1103/PhysRevLett.79.2554.

[11] Steven T. Bramwell and Michel J. P. Gingras. Spin ice state in frustrated magnetic pyrochlore materials. *Science*, 294(5546):1495–1501, 2001. doi: 10.1126/science.1064761. URL http://science.sciencemag.org/content/294/5546/1495.

[12] A.P. Ramirez, A. Hayashi, R.J. Cava, R. Siddarthan, and B.S. Shastry. Zero-point entropy in 'spin-ice'. *Nature*, 399:333–335, 1999.

[13] J. S. Gardner, S. R. Dunsiger, B. D. Gaulin, M. J. P. Gingras, J. E. Greedan, R. F. Kiefl, M. D. Lumsden, W. A. MacFarlane, N. P. Raju, J. E. Sonier, I. Swainson, and Z. Tun. Cooperative paramagnetism in the geometrically frustrated pyrochlore antiferromagnet $tb_2ti_2o_7$. *Phys. Rev. Lett.*, 82:1012–1015, Feb 1999. doi: 10.1103/PhysRevLett.82.1012. URL https://link.aps.org/doi/10.1103/PhysRevLett.82.1012.

[14] J.E. Greedan, M. Sato, Xu Yan, and F.S. Razavi. Spin-glass-like behavior in y2mo2o7, a concentrated, crystalline system with negligible apparent disorder. *Solid State Communications*, 59(12):895 – 897, 1986. ISSN 0038-1098. doi: http://dx.doi.org/10.1016/0038-1098(86)90652-6. URL http://www.sciencedirect.com/science/article/pii/0038109886906526.

[15] B. D. Gaulin, J. N. Reimers, T. E. Mason, J. E. Greedan, and Z. Tun. Spin freezing in the geometrically frustrated pyrochlore antiferromagnet $tb_2mo_2o_7$. *Phys. Rev.*

Lett., 69:3244–3247, Nov 1992. doi: 10.1103/PhysRevLett.69.3244. URL https://link.aps.org/doi/10.1103/PhysRevLett.69.3244.

[16] Jason S. Gardner, Michel J. P. Gingras, and John E. Greedan. Magnetic pyrochlore oxides. *Rev. Mod. Phys.*, 82:53–107, Jan 2010.

[17] Alannah M. Hallas, Jonathan Gaudet, and Bruce D. Gaulin. Experimental insights on ground state selection of quantum xy pyrochlores. 2017.

[18] A. M. Hallas, A. Z. Sharma, Y. Cai, T. J. Munsie, M. N. Wilson, M. Tachibana, C. R. Wiebe, and G. M. Luke. Relief of frustration in the heisenberg pyrochlore antiferromagnet $gd_2pt_2o_7$. *Phys. Rev. B*, 94:134417, Oct 2016. doi: 10.1103/PhysRevB.94.134417. URL https://link.aps.org/doi/10.1103/PhysRevB.94.134417.

[19] K. A. Ross, Th. Proffen, H. A. Dabkowska, J. A. Quilliam, L. R. Yaraskavitch, J. B. Kycia, and B. D. Gaulin. Lightly stuffed pyrochlore structure of single-crystalline $yb_2ti_2o_7$ grown by the optical floating zone technique. *Phys. Rev. B*, 86:174424, Nov 2012. doi: 10.1103/PhysRevB.86.174424. URL https://link.aps.org/doi/10.1103/PhysRevB.86.174424.

[20] S. V. Isakov, R. Moessner, S. L. Sondhi, and D. A. Tennant. Analytical theory for proton correlations in common-water ice I_h. *Phys. Rev. B*, 91:245152, Jun 2015. doi: 10.1103/PhysRevB.91.245152. URL https://link.aps.org/doi/10.1103/PhysRevB.91.245152.

[21] J. D. Bernal and R. H. Fowler. A theory of water and ionic solution, with particular reference to hydrogen and hydroxyl ions. *The Journal of Chemical Physics*, 1(8): 515–548, 1933. doi: 10.1063/1.1749327. URL http://dx.doi.org/10.1063/1.1749327.

[22] Linus Pauling. The structure and entropy of ice and of other crystals with some randomness of atomic arrangement. *Journal of the American Chemical Society*, 57 (12):2680–2684, 1935. doi: 10.1021/ja01315a102. URL http://dx.doi.org/10.1021/ja01315a102.

[23] M J P Gingras. Spin ice - a magnetic analogue of common water ice and a classical spin liquid. *Physics in Canada*, 68(2):89–94, 04 2012.

[24] J A Hodges, P Bonville, A Forget, M Rams, K Królas, and G Dhalenne. The crystal field and exchange interactions in yb 2 ti 2 o 7. *Journal of Physics: Condensed Matter*, 13(41):9301, 2001. URL http://stacks.iop.org/0953-8984/13/i=41/a=318.

[25] Papri Dasgupta, Yatramohan Jana, and Debjani Ghosh. Crystal field effect and geometric frustration in er2ti2o7 —an xy antiferromagnetic pyrochlore. *Solid State Communications*, 139(8):424 – 429, 2006. ISSN 0038-1098. doi: http://dx.doi.org/10.1016/j.ssc.2006.06.030. URL http://www.sciencedirect.com/science/article/pii/S0038109806005527.

[26] H. Cao, A. Gukasov, I. Mirebeau, P. Bonville, C. Decorse, and G. Dhalenne. Ising versus xy anisotropy in frustrated $R_2\mathrm{ti}_2\mathbf{o}_7$ compounds as "seen" by polarized neutrons. *Phys. Rev. Lett.*, 103:056402, Jul 2009. doi: 10.1103/PhysRevLett.103.056402. URL https://link.aps.org/doi/10.1103/PhysRevLett.103.056402.

[27] J. Gaudet, D. D. Maharaj, G. Sala, E. Kermarrec, K. A. Ross, H. A. Dabkowska, A. I. Kolesnikov, G. E. Granroth, and B. D. Gaulin. Neutron spectroscopic study of crystalline electric field excitations in stoichiometric and lightly stuffed $\mathrm{yb}_2\mathrm{ti}_2\mathrm{o}_7$. *Phys. Rev. B*, 92:134420, Oct 2015. doi: 10.1103/PhysRevB.92.134420. URL https://link.aps.org/doi/10.1103/PhysRevB.92.134420.

[28] A. M. Hallas, J. Gaudet, M. N. Wilson, T. J. Munsie, A. A. Aczel, M. B. Stone, R. S. Freitas, A. M. Arevalo-Lopez, J. P. Attfield, M. Tachibana, C. R. Wiebe, G. M. Luke, and B. D. Gaulin. Xy antiferromagnetic ground state in the effective $s = \frac{1}{2}$ pyrochlore $\mathrm{yb}_2\mathrm{ge}_2\mathrm{o}_7$. *Phys. Rev. B*, 93:104405, Mar 2016. doi: 10.1103/PhysRevB.93.104405. URL https://link.aps.org/doi/10.1103/PhysRevB.93.104405.

[29] Jonathan Gaudet, Alannah M. Hallas, N.P. Butch, Guangyong Xu, M. Tachibana, C.R. Wiebe, G.M Luke, and B.D. Gaul. Phase competition in the palmer-chalker ,xy pyrochlore $\mathrm{Er}_2\mathrm{Pt}_2\mathrm{O}_7$. 2017.

[30] J. D. M. Champion, M. J. Harris, P. C. W. Holdsworth, A. S. Wills, G. Balakrishnan, S. T. Bramwell, E. Čižmár, T. Fennell, J. S. Gardner, J. Lago, D. F. McMorrow, M. Orendáč, A. Orendáčová, D. McK. Paul, R. I. Smith, M. T. F. Telling, and A. Wildes. $\mathrm{er}_2\mathrm{ti}_2\mathrm{o}_7$:. *Phys. Rev. B*, 68:020401, Jul 2003. doi: 10.1103/PhysRevB.68.020401. URL https://link.aps.org/doi/10.1103/PhysRevB.68.020401.

[31] A Poole, A S Wills, and E Lelièvre-Berna. Magnetic ordering in the xy pyrochlore antiferromagnet er 2 ti 2 o 7 : a spherical neutron polarimetry study. *Journal of Physics: Condensed Matter*, 19(45):452201, 2007. URL `http://stacks.iop.org/0953-8984/19/i=45/a=452201`.

[32] Henry R Hoekstra and F Gallagher. Synthesis of some pyrochlore-type oxides of platinum (iv) at high pressure. *Inorganic Chemistry*, 7(12):2553–2557, 1968.

[33] R. D. Shannon. Revised effective ionic radii and systematic studies of interatomic distances in halides and chalcogenides. *Acta Crystallographica Section A*, 32(5): 751–767, Sep 1976.

[34] C. R. Wiebe and A. M. Hallas. Frustration under pressure: Exotic magnetism in new pyrochlore oxides. *APL Materials*, 3(4):041519, 2015. doi: 10.1063/1.4916020.

[35] Y. Q. Cai, Q. Cui, X. Li, Z. L. Dun, J. Ma, C. dela Cruz, Y. Y. Jiao, J. Liao, P. J. Sun, Y. Q. Li, J. S. Zhou, J. B. Goodenough, H. D. Zhou, and J.-G. Cheng. High-pressure synthesis and characterization of the effective pseudospin $s = 1/2$ xy pyrochlores $r_2Pt_2o_7$ (r = Er, Yb). *Phys. Rev. B*, 93:014443, Jan 2016.

[36] Kate A. Ross, Lucile Savary, Bruce D. Gaulin, and Leon Balents. Quantum excitations in quantum spin ice. *Phys. Rev. X*, 1:021002, Oct 2011. doi: 10.1103/PhysRevX.1.021002. URL `https://link.aps.org/doi/10.1103/PhysRevX.1.021002`.

[37] JD Thompson, PA McClarty, D Prabhakaran, I Cabrera, T Guidi, and R Coldea. Quasiparticle breakdown and spin hamiltonian of the frustrated quantum pyrochlore $Yb_2Ti_2O_7$ in magnetic field. *arXiv preprint arXiv:1703.04506*, 2017.

[38] Lucile Savary, Kate A. Ross, Bruce D. Gaulin, Jacob P. C. Ruff, and Leon Balents. Order by quantum disorder in $Er_2Ti_2O_7$. *Phys. Rev. Lett.*, 109:167201, Oct 2012. doi: 10.1103/PhysRevLett.109.167201. URL `https://link.aps.org/doi/10.1103/PhysRevLett.109.167201`.

[39] L. D. C. Jaubert, Owen Benton, Jeffrey G. Rau, J. Oitmaa, R. R. P. Singh, Nic Shannon, and Michel J. P. Gingras. Are multiphase competition and order by disorder the keys to understanding $yb_2ti_2o_7$? *Phys. Rev. Lett.*, 115:267208, Dec 2015. doi: 10.1103/PhysRevLett.115.267208. URL `https://link.aps.org/doi/10.1103/PhysRevLett.115.267208`.

[40] Robert C Weast, 1928 Lide, David R., and University of Rhode Island. Coastal Resources Center. *CRC handbook of chemistry and physics*. Cleveland, Ohio : CRC Press, 1978. "A ready-reference book of chemical and physical data.".

[41] Hironori Sakai, Masaki Kato, Kazuyoshi Yoshimura, and Koji Kosuge. Tl-nmr study of pyrochlore oxide tl2ru2o7: Observation of spin-singlet formation. *Journal of the Physical Society of Japan*, 71(2):422–424, 2002. doi: 10.1143/JPSJ.71.422. URL `http://dx.doi.org/10.1143/JPSJ.71.422`.

[42] Hironori Sakai, Kazuyoshi Yoshimura, Harukazu Kato, Shinsaku Kambe, and Russell E Walstedt. Nmr study of metallic pyrochlore ruthenium oxides, $Bi_2Ru_2O_7$ and $Pb_2Ru_2O_7$. *Journal of Physics and Chemistry of Solids*, 63(6):1039 – 1041, 2002. ISSN 0022-3697. doi: http://dx.doi.org/10.1016/S0022-3697(02)00025-2. Proceedings of the 8th ISSP International Symposium.

[43] O Vyaselev, K Kobayashi, K Arai, J Yamazaki, K Kodama, M Takigawa, M Hanawa, and Z Hiroi. Cd and re nmr/nqr in pyrochlore compound cd2re2o7. *Journal of Physics and Chemistry of Solids*, 63(6):1031 – 1034, 2002. ISSN 0022-3697. doi: http://dx.doi.org/10.1016/S0022-3697(02)00004-5. URL `http://www.sciencedirect.com/science/article/pii/S0022369702000045`. Proceedings of the 8th ISSP International Symposium.

[44] J. A. Hodges, P. Bonville, A. Forget, A. Yaouanc, P. Dalmas de Réotier, G. André, M. Rams, K. Królas, C. Ritter, P. C. M. Gubbens, C. T. Kaiser, P. J. C. King, and C. Baines. First-order transition in the spin dynamics of geometrically frustrated $yb_2ti_2O_7$. *Phys. Rev. Lett.*, 88:077204, Feb 2002. doi: 10.1103/PhysRevLett.88.077204. URL `https://link.aps.org/doi/10.1103/PhysRevLett.88.077204`.

[45] A. Yaouanc, P. Dalmas de Réotier, P. Bonville, J. A. Hodges, V. Glazkov, L. Keller, V. Sikolenko, M. Bartkowiak, A. Amato, C. Baines, P. J. C. King, P. C. M. Gubbens, and A. Forget. Dynamical splayed ferromagnetic ground state in the quantum spin ice $yb_2sn_2\mathbf{o}_7$. *Phys. Rev. Lett.*, 110:127207, Mar 2013. doi: 10.1103/PhysRevLett.110.127207. URL `https://link.aps.org/doi/10.1103/PhysRevLett.110.127207`.

[46] Z. L. Dun, M. Lee, E. S. Choi, A. M. Hallas, C. R. Wiebe, J. S. Gardner, E. Arrighi, R. S. Freitas, A. M. Arevalo-Lopez, J. P. Attfield, H. D. Zhou, and J. G. Cheng.

Chemical pressure effects on magnetism in the quantum spin liquid candidates $yb_2X_2o_7$ (x = Sn, ti, ge). *Phys. Rev. B*, 89:064401, Feb 2014. doi: 10.1103/PhysRevB.89.064401. URL `https://link.aps.org/doi/10.1103/PhysRevB.89.064401`.

[47] Robert D'Ortenzio. *Ground State of the Quantum Spin Ice $Yb_2Ti_2O_7$*. PhD thesis, McMaster University, 2013.

[48] Charles Slichter. *Principles of Magnetic Resonance*. Springer, 1996.

[49] N.W. Ashcroft and N.D. Mermin. *Solid State Physics*. Saunders College, Philadelphia, 1976.

[50] J. Winter. *Magnetic resonance in metals*. International series of monographs on physics. Clarendon Press, 1971.

[51] N. Bloembergen and T.J. Rowland. On the nuclear magnetic resonance in metals and alloys. *Acta Metallurgica*, 1(6):731 – 746, 1953.

[52] Tôru Moriya. The effect of electron-electron interaction on the nuclear spin relaxation in metals. *Journal of the Physical Society of Japan*, 18(4):516–520, 1963.

[53] F. Mila and T.M. Rice. Analysis of magnetic resonance experiments in yba2cu3o7. *Physica C: Superconductivity*, 157(3):561 – 570, 1989.

[54] V. Jaccarino. Theory of magnetism in transition metals. ed. W. Marshall, 1967.